UNIVERSITY OF CALIFORNIA, SAN DIEGO

Using Amines and Alkanes as Thermal-Runaway Retardants for Lithium-Ion Battery

A dissertation submitted in partial satisfaction of the
requirements for the degree Doctor of Philosophy

in

Materials Science and Engineering

by

Yang Shi

Committee in Charge:

Professor Yu Qiao, Chair
Professor Prabhakar R. Bandaru
Professor Renkun Chen
Professor Jian Luo
Professor Ying Shirley Meng

2016

The dissertation of Yang Shi is approved, and it is acceptable in quality and form for publication on microfilm and electronically:

Chair

University of California, San Diego

2016

DEDICATION

This dissertation is dedicated to my parents.

EPIGRAPH

Science is but a perversion of itself

unless it has as its ultimate goal the betterment of humanity.

- Nikola Tesla, 1919

TABLE OF CONTENTS

LIST OF FIGURES

LIST OF TABLES

ACKNOWLEDGEMENTS

First of all, I would like to express my sincere gratitude to my advisor, Professor Yu Qiao for his continuous support and guidance of my PhD study and research. This dissertation could not have been completed without the great support that I received from him. I am deeply impressed with his patience and immense knowledge. His valuable guidance helped me through my entire research and writing of this dissertation. In addition, I would like to thank my committee members: Professor Jian Luo, Professor Prabhakar R. Bandaru, Professor Renkun Chen, and Professor Ying Shirley Meng, for their valuable time and suggestions.

Secondly, I would like to thank my colleagues working on the battery project, Daniel J. Noelle, Meng Wang, and Anh V. Le. I received tremendous help from them and had many useful and inspiring discussions with them. I'm also grateful to other group members in the Multifunctional Materials Research Laboratory (MMRL) who have helped and inspired me: Dr. Weiyi Lu, Dr. Hyuck Lim, Dr. Cang Zhao, Dr. Tzehan Chen and Brian J. Chow. In addition, thanks are also due to the collaborators in the Laboratory for Energy Storage and Conversion (LESC): Dr. Hyojung Yoon, Minghao Zhang, and Hyeseung Chung, for their invaluable help throughout the projects.

Finally, I would like to express my special thanks to Ms. Lindsay Walton, who has always been very helpful for administrative issues.

Chapter 3, in full, is a reprint of the material "Exothermic behaviors of

mechanically abused lithium-ion batteries with dibenzylamine" as it appears in the Journal of Power Sources, Yang Shi, Daniel J. Noelle, Meng Wang, Anh V. Le, Hyojung Yoon, Minghao Zhang, Ying Shirley Meng, Yu Qiao, 2016, 326, 514-521. The dissertation author was the first author of this paper and conducted all the essential research work.

Chapter 4, in full, is a reprint of the material "Roles of amines for thermal-runaway-mitigating lithium-ion battery" as it appears in ACS Applied Materials and Interfaces, Yang Shi, Daniel J. Noelle, Meng Wang, Anh V. Le, Hyojung Yoon, Minghao Zhang, Ying Shirley Meng, Yu Qiao, 2016, 8, 30956-30963. The dissertation author was the first author of this paper and conducted all the essential research work.

Chapter 5, in part, is currently being submitted for publication of the material "Mitigating thermal runaway of lithium-ion battery through electrolyte displacement", Yang Shi, Daniel J. Noelle, Meng Wang, Anh V. Le, Hyojung Yoon, Minghao Zhang, Ying Shirley Meng, Jiang Fan, Dengguo Wu, Yu Qiao, 2016. The dissertation author was the first author of this paper and conducted all the essential research work.

I would like to acknowledge the financial support from the Advanced Research Projects Agency - Energy (ARPA-E).

VITA

2012	B.S., Materials Science and Engineering, Dalian University of Technology, Dalian, China
2013	M.S., Materials Science and Engineering, University of California – San Diego, La Jolla, CA
2016	Ph.D., Materials Science and Engineering, University of California – San Diego, La Jolla, CA

PUBLICATIONS

1. Kim, H., Khamwannah, J., Choi, C., **Shi, Y.** and Jin, S., 2013. Hydrothermally grown TiO 2 nanotubes on multi-layered Ti mesh electrodes for enhanced photoelectrochemical reaction. MRS Communications, 3(04), pp.235-240.

2. Lim, H., **Shi, Y.**, Wang, M. and Qiao, Y., 2015. Effects of work function on thermal sensitivity of electrode potential. Applied Physics Letters, 106(22), p.223901.

3. Le, A.V., Wang, M., **Shi, Y.**, Noelle, D.J. and Qiao, Y., 2015. Heat generation of mechanically abused lithium-ion batteries modified by carbon black micro-particulates. Journal of Physics D: Applied Physics, 48(38), p.385501.

4. Le, A.V., Wang, M., **Shi, Y.**, Noelle, D., Qiao, Y. and Lu, W., 2015. Effects of additional multiwall carbon nanotubes on impact behaviors of LiNi0. 5Mn0. 3Co0. 2O2 battery electrodes. Journal of Applied Physics, 118(8), p.085312.

5. Chen, T., Chow, B.J., Wang, M., **Shi, Y.**, Zhao, C. and Qiao, Y., 2015. Inorganic–organic hybrid of lunar soil simulant and polyethylene. Journal of Materials in Civil Engineering, 28(4), p.06015013.

6. Zhao, C., Wang, M., **Shi, Y.**, Cao, J. and Qiao, Y., 2016. High-temperature post-processing treatment of silica nanofoams of controlled pore sizes and porosities. Materials & Design, 90, pp.815-819.

7. Lim, H., **Shi, Y.** and Qiao, Y., 2016. Thermally chargeable supercapacitor working in a homogeneous, changing temperature field. Applied Physics A, 122(4), pp.1-6.

8. **Shi, Y.**, Zhang, M., Qian, D. and Meng, Y.S., 2016. Ultrathin Al 2 O 3 Coatings for improved cycling performance and thermal stability of $LiNi_{0.5}Co_{0.2}Mn_{0.3}O_2$ Cathode Material. Electrochimica Acta, 203, pp.154-161.

9. **Shi, Y.**, Noelle, D.J., Wang, M., Le, A.V., Yoon, H., Zhang, M., Meng, Y.S. and Qiao, Y., 2016. Exothermic behaviors of mechanically abused lithium-ion batteries with dibenzylamine. Journal of Power Sources, 326, pp.514-521.

10. Wang, M., Le, A.V., Noelle, D.J., **Shi, Y.**, Yoon, H., Zhang, M., Meng, Y.S. and Qiao, Y., 2016. Effects of electrode pattern on thermal runaway of lithium-ion battery. International Journal of Damage Mechanics, p.1056789516660176.

11. Wang, M., Le, A.V., **Shi, Y**., Noelle, D. J., Yoon, H., Zhang, M., Meng, Y.S. and Qiao, Y., 2016. Effects of angular fillers on thermal runaway of lithium-ion battery. Journal of Materials Science & Technology, in press

12. **Shi, Y.**, Noelle, D.J., Wang, M., Le, A.V., Yoon, H., Zhang, M., Meng, Y.S. and Qiao, Y., 2016. Roles of amines in thermal-runaway-mitigating lithium-ion battery. ACS Applied Materials & Interfaces, 8, pp. 30956-30963

13. **Shi, Y.**, Noelle, D.J., Wang, M., Le, A.V., Yoon, H., Zhang, M., Meng, Y.S., Fan, J., Wu, D., and Qiao, Y., 2016. Mitigating thermal runaway of lithium-ion battery through electrolyte displacement, submitted

ABSTRACT OF THE DISSERTATION

Using Amines and Alkanes as Thermal-Runaway Retardants for Lithium-Ion Battery

by

Yang Shi

Doctor of Philosophy in Materials Science and Engineering

University of California, San Diego, 2016

Professor Yu Qiao, Chair

Thermal runaway imposes major challenges to large-scale lithium-ion batteries (LIBs). The working temperature of a LIB is usually around room temperature. However, upon mechanical abuse such as an impact or nail penetration, LIB cell components may fail and internal short circuits could be formed. As a result, a series of exothermic electrochemical reactions and decompositions would take place and the local temperature can rapidly increase.

In this thesis, a few novel techniques are investigated to mitigate thermal runaway of LIBs. Mechanically triggered approach has been employed. Thermal-runaway retardant (TRR) is encapsulated in mechanically responsive packages made of materials inert to the battery environment, and upon external mechanical loadings the packages can be broken apart and release the TRR. This mechanism allows for the use of aggressive chemicals to suppress the short circuit discharge and reduce the subsequent exothermic phenomena, immediately after the battery is damaged even before temperature increase begins.

The best TRR candidates are identified to be amines and alkanes. Among amines, secondary amines and tertiary amines perform better than primary amines. The reduction in electrolyte ionic conductivity and the displacement of electrolyte are the thermal-runaway-mitigation mechanisms of the secondary and the tertiary amines, respectively. Pentadecane is the best candidate among the alkanes under investigation, with the major working mechanism being electrolyte displacement. Impact tests on large pouch cells and high-energy battery chemistry were also performed; the results were quite encouraging.

Chapter 1. Introduction

1.1. Safety Issues of Lithium Ion Battery

Lithium ion battery (LIB) receives increasing attention as an attractive solution for electric vehicles (EV), hybrid electric vehicles (HEV), and plug-in hybrid electric vehicles (PHEV). With higher-energy-density active materials being developed, safety and robustness of LIB cells, modules, and packs impose tough challenges to vehicle system design.

LIB combines highly energetic materials in contact with a highly volatile flammable electrolyte. They can suffer catastrophic failure if subjected to unexpected mechanical or thermal abuses. Overheating, overcharging, external short circuiting, or crushing can trigger spontaneous heat-evolving reactions that can rapidly lead to fire or even explosion [1].

1.2. Failure Modes of LIB and Mechanisms

1.2.1. Elevated temperatures

1.2.1.1. Decomposition of Solid Electrolyte Interface

Solid electrolyte interphase (SEI) is an electronically insulating but ionically conducting film typically formed at the negative electrode during charging. SEI growth

results from electrochemical decomposition of the electrolyte. The product forms a solid layer on the surface of the active material [2].

The first stage of failure of a LIB cell upon internal shorting is the breakdown of SEI layer on anode, due to overheating or physical penetration. The SEI film contains both stable (such as LiF and Li2CO3) and metastable components (such as ROCO2Li, (CH2OCO2Li)2 and ROLi); the latter decomposes exothermically when the temperature is between 90 °C to 120 °C: [3].

$$(CH_2OCO_2Li)_2 \rightarrow Li_2CO_3 + C_2H_4 + CO_2 + 1/2\ O_2$$

$$2Li + (CH_2OCO_2Li)_2 \rightarrow 2Li_2CO_3 + C_2H_4$$

Yang et al [4] postulated a possible reaction pathway (**Figure 1.1**) leading to the thermal runaway of LIB. Once the battery reaches approximately 85 °C, SEI on the graphite negative electrode begins to exothermically decompose. If the temperature increases to 110 °C, a secondary film begins to form and decompose. Evolution of O2 from charged cathode starts at 225 °C. The negative electrode graphite reacts at 330 °C, releasing additional heat. Eventually, the aluminum current collector can be melted at 660 °C. The scenario can be quite dangerous especially for large systems [5].

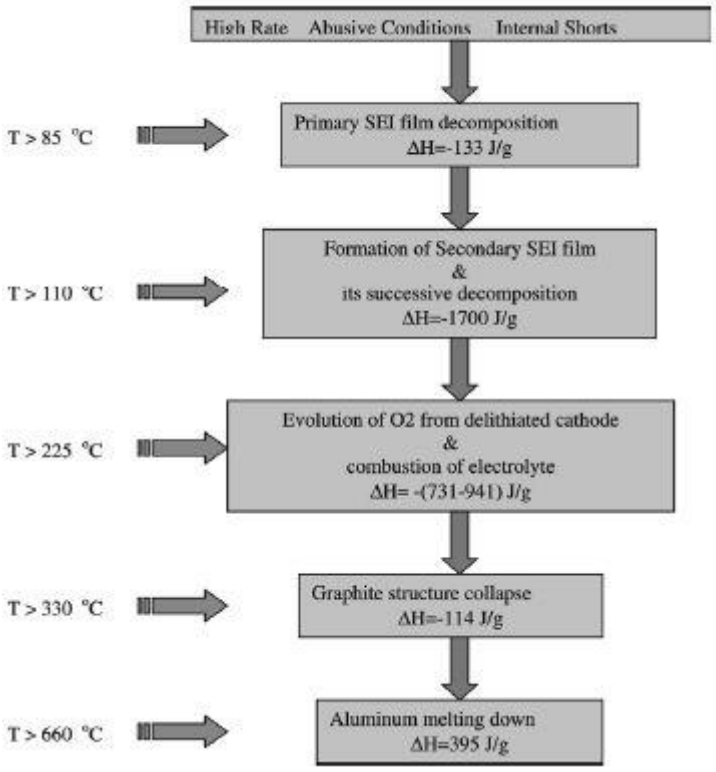

Figure 1.1 A conceptual roadmap leading to the thermal runaway in LIB

1.2.1.2. Reaction of intercalated Li with electrolyte

Organic solvents used in the electrolyte might react with lithium [3].

$$2Li + C_3H_4O_3 \text{ (EC)} \rightarrow Li_2CO_3 + C_2H_4$$

$$2Li + C_4H_6O_3 \text{ (PC)} \rightarrow Li_2CO_3 + C_3H_6$$

$$2Li + C_3H_6O_3 \text{ (DMC)} \rightarrow Li_2CO_3 + C_2H_6$$

These reactions release flammable hydrocarbon gases, which causes pressure to build up inside the cell. The reaction typically starts at 100 °C but with some electrolytes it can be as low as 68 °C [6-7]. Before oxygen is released from the cathode material, the gases usually do not burn, even when the temperature increases to beyond the flashpoint.

1.2.1.3. Decomposition of salts in electrolytes

Electrolytes currently used in LIB consist of lithium ion (Li^+) and large anions such as PF_6^-. $LiPF_6$ salt is thermally unstable in the solid state and decomposes to LiF and PF_5 [8-9], a reaction that gets accelerated in the presence of organic solvents [1]. PF_5 hydrolyzes to form HF and PF_3O, which react with both the cathode and anode, deteriorating cell performance [10]. In addition, due to temperature rising and the thermodynamic instability of these anions, the reduction reaction with Li can produce a large amount of heat [4].

1.2.1.4. Cathode active material decomposition and reaction with electrolytes

At around 130 °C the separator melts, which can result in internal shorting between the electrodes. Eventually, heat from the breakdown of electrolyte causes breakdown of the cathode material, releasing oxygen which enables burning of both the electrolyte and the gases accumulated inside the cell.

1.2.2. Overcharge and over discharge

When voltage exceeds the upper limit, excess Li^+ de-intercalation will cause irreversible phase transitions and collapse of the cathode. When Li-intercalation in graphite exceeds the designed value, Li dendrites might lead to internal short circuit [1].

1.2.3. Internal short circuit

Dendrite lithium that grows on the surface of anode will puncture the separator and connect the positive and negative electrodes, leading to short circuit of LIB. In addition, external causes such as mechanical damage, over charge and over discharge could also lead to formation of internal short circuit. Internal short circuit instantly generate a huge current, causing rapid increase of heat generation.

1.3. Existing Solutions for Safety Issues

1.3.1. Coating on electrode

1.3.1.1. Coating on cathode

When the surface of cathode materials, such as $LiCoO_2$, $LiNiO_2$, $LiMn_2O_4$ and $LiMnO_2$, are coated with oxides, such as MgO, Al_2O_3, SiO_2, TiO_2, ZnO, SnO_2, and ZrO_2, the coating prevents the direct contact with the electrolyte solution, suppresses phase transition, improves the structural stability, and decreases the disorder of cations in crystal sites [3].

Cho et al. reported an improvement in both thermal stability and electrochemical properties of $LiCoO_2$ cathodes by applying a direct coating of $AlPO_4$ nanoparticles from

an aqueous solution [10]. Similar improvements had been achieved in $LiNi_{0.8}Co_{0.1}Mn_{0.1}O_2$ cathode as well [11]. Kweon et al. studied the effect of MgO and Al_2O_3 coatings on the thermal stability of $LiCoO_2$ cathode [12]. Yang et al. found that the overcharge tolerance of $MnSiO_4$ coated cathode was better than that of pristine $LiCoO_2$ cathode [13]. Xia et al. synthesized a temperature-sensitive cathode material, $LiCoO_2$-P3DT, which has a thermal shutdown action at an elevated temperature of 110°C, providing a thermally triggered protection [14].

1.3.1.2. Coating on anode

Thermal decomposition of SEI can be relatively easily triggered. Therefore, improving the thermal stability of SEI is an important approach to enhance the safety of the anode. SEI can be modified by mild oxidation, deposition of metals and metal oxides, coating with polymers or other carbon materials. As a result, direct contact of graphite with the electrolyte is prevented, and the decomposition of electrolytes is suppressed[3].

Park et al. investigated the effect of non-graphitic carbon coatings on the thermal stability of graphite at elevated temperature [15]. DSC studies show that the thermal stability of the surface-modified graphite electrode is improved.

Coatings on electrodes could increase the thermal stability of charged electrodes, evidenced by the delay of exothermic peaks in DSC. However, extensive fundamental study is still needed to enhance their efficiency.

1.3.2. Additives in electrolyte

1.3.2.1. Fire retardant additives

Most fire retardant additives are organic phosphorus compounds and their halogenated derivatives. Most of the non-phosphorus is fluorinated propylene carbonates and methyl nonafluorobuyl ether.

Table 1.1 shows the mechanism of different fire retardant additives. **Table 1.2** shows a list of fire retardants that people have investigated as potential additives in LIB cells.

Table 1.1 Mechanisms of different fire retardant additives

Flame retardant	**Mechanism**
Br/Cl containing	HBr/HCl reacts with OH radical, retards the combustion chain reaction
P containing	Form phosphoric acid by thermal degradation, dehydrate polymer underneath (form protective char layer), also form P and PO radicals, interrupting radical chain of combustion
N containing	Release of inert gases (ammonia, nitrogen) into the gas phase (dilute)
Inorganic	Mainly $Al(OH)_3$/$Mg(OH)_2$, endothermic reaction when decompose to metal oxide, cooling polymer, dilution of the substrate and gases, only physical action, no chemical action

Table 1.2 List of existing fire retardant additives

Name	Reference
Phosphate/Phosphonate	
Triphenylphosphate (TPP)	[16]
Vinyl ethylene carbonate (VEC) + biphenyl (BP) + TPP	[17]
Dimethyl methylphosphonate (DMMP)	[18-19]
Triphenyl phosphate (TPP)	[17, 20-23]
Tris(trifluoroethyl)phosphate (TFP)	[24-26]
Phosphorus-containing esters	[27]
Methoxyethoxyethoxyphosphazenes	[28]
Bis(N,N-diethyl)methoxyethoxymethylphosphonamidate	[29]
Triphenyl Phosphate (TPP), Trinutyl Phosphate (TBP)	[30]
Trimethyl Phosphate (TMP), Triethyl Phosphate (TEP)	[31]
Ethylene Ethyl Phosphate(EEP) + TMP	[32]
Diphenyloctyl phosphate(DPLP)	[33]
Cyclic phosphate	[34]
Phosphites	
Tris(2,2,2-Trifluoroethyl) Phosphite (TTFP)	[35-36]
Triethyl and Tributyl Phosphite	[37]
Trimethyl phosphite (TMP)	[38]
Phosphazenes	
Ethyleneoxy Phosphazenes	[28]
Phosphazene-based flame retardants	[39]
Hexamethoxycyclotriphosphazene	[40]
Miscellaneous compounds	
Hexamethylphosphoramide (HMPA)	[41]
Dimethyl Methylphosphonate (DMMP)	[42]

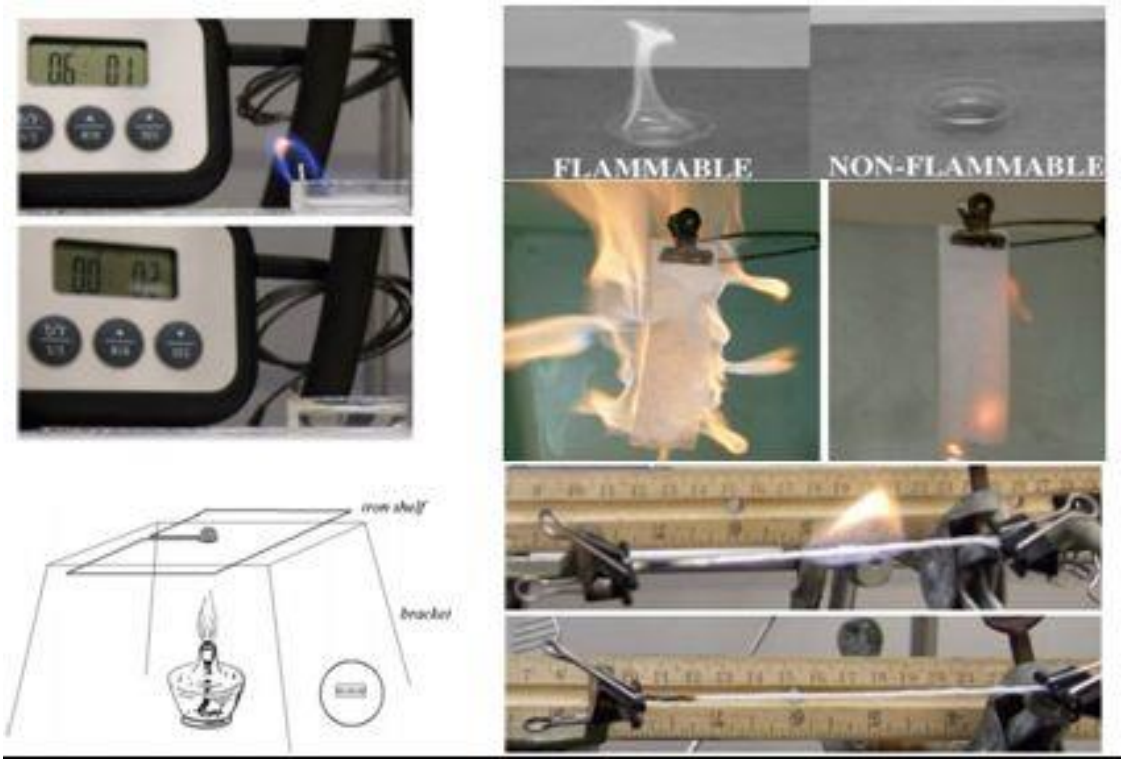

Figure 1.2 Self-extinguishing time measurement

To test the influence of fire retardant additives, several characterization methods were used, including self-extinguishing time measurement, DSC test, ionic conductivity measurement and electrochemical performance test. **Figure 1.2** shows several self-extinguishing time test setups [28, 39, 43-45]. Unfortunately the reduction in flammability with the addition of these flame retardant additives has to be realized at the expense of ionic conductivity of the electrolyte and electrochemical performance of the cell.

1.3.2.2. Redox shuttles

During overcharge, the oxidation reaction of the redox shuttle first occurs, rather

than oxidation and decomposition of electrolyte on the surface of cathode. Then, the oxidized state of the shuttle quickly diffuses to the anode, reduces to its original state, and shuttles back to the cathode. Through this mechanism, the potential of the cathode is locked at the oxidation potential of the redox shuttle molecules [46]. A typical way to screen redox shuttle additives is cyclic voltammetry (CV). However, the effectiveness of the shuttle molecules was not sustained with cycling [46].

1.3.2.3. Shutdown additives

Baginska et al. developed a thermally triggered shutdown mechanism of LIB by incorporating thermoresponsive polymer microspheres onto battery anodes or separators [47]. When the internal battery environment reaches a critical temperature, the microspheres melt and coat the anode/separator with a nonconductive barrier, halting Li^+ transport and shutting down the reactions. Xia et al. investigated a thermally polymerizable monomer, 1,1'-(methylenedi-4,1-phenylene) bismaleimide (BMI) as a safety electrolyte additive [48]. The BMI additive solidifies the electrolyte at 110 °C, which can block the Li^+ transport between electrodes.

1.3.3. Positive temperature coefficient material

Feng et al. prepared a positive temperature coefficient (PTC) electrode by coating a thin layer of epoxy-carbon material between the $LiCoO_2$ layer and the current collector

[49]. When the battery was overheated, the resistance of the PTC layer increased enormously and shut down the LIB. Kise et al. prepared a PTC compound as the conductive material, and the resistivity of PTC cathodes increased several-fold from 130 to 140 °C [50]. An overcharge test was also carried out and the cell temperature did not shoot up due to the increased cell impedance [51]. Zhong et al. proposed and fabricated an ethylene vinyl acetate (EVA) based PTC material with a transition temperature of 90 °C [52]. In spite of the encouraging results, it is well known that the thermally triggered mechanism only take actions after the temperature is reaching the threshold value of accelerated heating.

1.3.4. Safety devices

There are mainly three kinds of safety devices. The first category is safety vents. If the pressure inside a cell builds up, a plastic laminate membrane is punctured by a spike incorporated in the vent, releasing internal pressure. The second category is thermal fuses, which is a wire of a fusible alloy that melts when a pre-set current flows through it. The third category is shutdown separators. If the cell temperature rises abnormally, the heat generated softens the separators and closes the pores.

1.4. Motivation and Outline of the Thesis

Safety and robustness is a “bottleneck” to wider applications of large-scale LIB cells in EV, smart grid, etc, especially when the specific energy of LIB is rapidly improved.

As discussed above, although a number of approaches have been proposed to address this issue, currently efficient and reliable thermal-runaway mitigation (TRM) techniques are still lacking.

In this thesis, a new concept of mechanically triggered TRM mechanism will be systematically investigated. A thermal runaway retardant (TRR) is encapsulated in packages made of inert materials. When the LIB is subjected to mechanical abuse, the packages are broken apart and the TRR is released, which suppresses Li^+ transport.

Chapter 2 describes the selection of TRR candidates. **Chapter 3** shows how a promising TRR candidate, dibenzylamine, works successfully in large-capacity coin cells. The nail penetration test and impact test performances of modified cells were compared with reference cells, and the working mechanism of dibenzylamine was investigated. **Chapter 4** explores other amines, leading to a deeper understanding of the working mechanisms of TRR. **Chapter 5** shows the performance of the best TRR candidate - pentadecane in pouch cells, with the working mechanism and the wetting speed being investigated. **Chapter 6** shows the ongoing work on the performance of TRR in LIB cells with high-energy-density Li-excess cathode. **Chapter 7** summarizes the overall work and discusses plans for future research.

Chapter 2. Selection of Thermal-Runaway Retardants

The criteria of the selection of thermal-runaway retardants (TRR) include efficacy, efficiency, flammability, and toxicity. A promising TRR should suppress Li^+ transport efficiently immediately after it is released, and it should not be highly flammable and acutely toxic. After the initial screening, possible TRR candidates are classified into a few groups according to their possible working mechanisms, as shown in **Table 2.1**. These TRR were tested to evaluate the efficiency on temperature reduction in nail penetration tests, discussed below.

Table 2.1 TRR candidates classification

Possible working mechanisms	Classes	Candidates
Fire extinguishing additives	Carbonate	Sodium bicarbonate
Electrolyte superabsorbents	Polymer	Poly(ethylene oxide)
Gas-generation agents	Hydrazide	2-hydroxyethylhydrazine, formic hydrazide, carbohydrazide
Solvation-shell interruption agents	Lewis bases	Benzylamine, dibenzylamine, trihexylamine
Electrolyte-displacement agents	Alkanes	Octane, pentadecane, icosane

2.1. Fire Extinguishing Additives

Sodium bicarbonate is a common fire extinguishing agent used as the dry chemical in fire extinguishers. Fine sodium bicarbonate powder is known to be effective and fast decomposing, which can generate a relatively large amount of carbon dioxide and absorb much heat in a limited period of time.

2.1.1. Experimental

Solvent of LIB electrolyte, dimethyl carbonate (DMC) was chosen as the liquid fuel. Sodium bicarbonate particles less than 20μm were harvested through sieve analysis. A 12’’×12’’ ×12’’ combustion chamber was constructed by using borosilicate glass. Two watch glasses with diameter of 100 mm were used as the containers of electrolyte and sodium bicarbonate particles. The setup is shown in **Figure 2.1**.

Figure 2.1 Flammability test setup

Several experiments were performed: (1) 1 ml DMC on a watch glass was ignited by a match, with or without 0.3-3g sodium bicarbonate, as the chamber was closed; (2) 4 ml DMC on a watch glass was ignited, with or without 0.3-3g sodium bicarbonate, as the chamber was open and a smooth air flow above the flame was provided; (3) 4 ml DMC on a watch glass was ignited in the open chamber, and sodium bicarbonate was added during the combustion; (4) 1 ml DMC on a watch glass was ignited, nitrogen was purged

into the chamber as it was closed. The flame extinguishing time was recorded and each procedure was repeated for 10 times.

2.1.2. Results and Discussion

DMC without sodium bicarbonate had blue flame, while DMC with sodium bicarbonate had yellow flame due to the presence of sodium ions. **Figure 2.2** shows the flames of DMC with and without sodium bicarbonate. However, there is no difference in the combustion time between DMC samples with and without sodium bicarbonate. Both were extinguished only after the liquid fuel had been exhausted.

Figure 2.2 DMC flame without (left) and with sodium bicarbonate (right)

4 ml DMC without any additives could spontaneously extinguish in a closed chamber. In order to let the flame last long enough to reach high temperature to promote the decomposition of sodium bicarbonate, the chamber must be kept open and a smooth

air flow should be maintained. However, there is still no difference in the combustion times between DMC with and without sodium bicarbonate. Both flames could last until the fuel had been exhausted. After combustion, sodium bicarbonate particles left on the watch glass were studied by TGA. TGA data showed that an average of 33.75% of sodium bicarbonate had decomposed during the combustion.

To simulate the fire extinguishing behavior or sodium bicarbonate in real fire extinguishers, sodium bicarbonate particles were added during the combustion process. Whenever the particles were introduced, the flame showed bright yellow color, but the fire could not be extinguished with up to 3 g of sodium bicarbonate.

In order to evaluate the critical oxygen concentration to extinguish the fire, nitrogen was introduced into the chamber to estimate the minimum amount of required sodium bicarbonate. About 1000 mL nitrogen would result in extinguishment of the fire before DMC was exhausted, suggesting that 0.045 mole carbon dioxide should be generated by sodium bicarbonate. That is, ~7.5 g sodium bicarbonate must be used to extinguish the fire of 1 ml DMC in a closed chamber. In a type-2016 coin cell, about 0.2 ml electrolyte is used, which demands ~1.5 g sodium bicarbonate (with the assumed 100% decomposition efficiency). Note that the mass of electrode is only less than 0.5 g.

It is clear that fire-extinguishing chemicals in dry powder fire extinguishers, such as sodium bicarbonate, monoammonium phosphate, potassium bicarbonate, potassium bicarbonate and potassium chloride, are not proper candidates. Once the fire is on, it is

difficult to put it out, or even suppress it by using chemicals additives. One of the reasons might be the low decomposition rate. Fine particles could reach a high temperature rapidly. During combustion, however, fine particles tend to be fused together, reducing the effective surface area.

2.2. Electrolyte Superabsorbent

Electrolyte is used to conduct Li^+ in LIB. If the electrolyte could be absorbed by a superabsorbent, the Li^+ transport would be suppressed and the thermal runaway reactions could be mitigated.

2.2.1. Experiments

Cathode active material ($LiNi_{0.5}Co_{0.2}Mn_{0.3}O_2$, NCM 523) and anode active material (graphite) were made into type-2016 half cells with Li metal as the counter electrode. Different amount of electrolyte was added. All the half cells were cycled at 1C (1C=200 mA g^{-1}) rate.

3 wt% poly (ethylene oxide) (PEO) containing electrode was processed with a mass loading of 20 mg/cm^2. Cathode half cells were assembled. 30 μL electrolyte was added in the reference and 3 wt% PEO modified cell. Nail penetration tests of charged coin cells were carried out. The stainless steel nail has a diameter of 2 mm.

2.2.2. Results and Discussion

In NCM523/Li half cells, for an active material mass loading of 10±0.5 mg, when 10 µl electrolyte (5 µl for each side) is added, the cells show the theoretical discharge capacity and acceptable fading in capacity during the first 20 cycles. When the amount of electrolyte is decreased to 4 µl (2 µl for each side), the cells show 1/3 of normal discharge capacity in the first discharge cycle. Serious fading is observed during the subsequent 19 cycle, showing almost no capacity in the 20th cycle. The comparison in discharge capacity for 4-µl and 10-µl electrolyte half cells is shown in **Figure 2.3**.

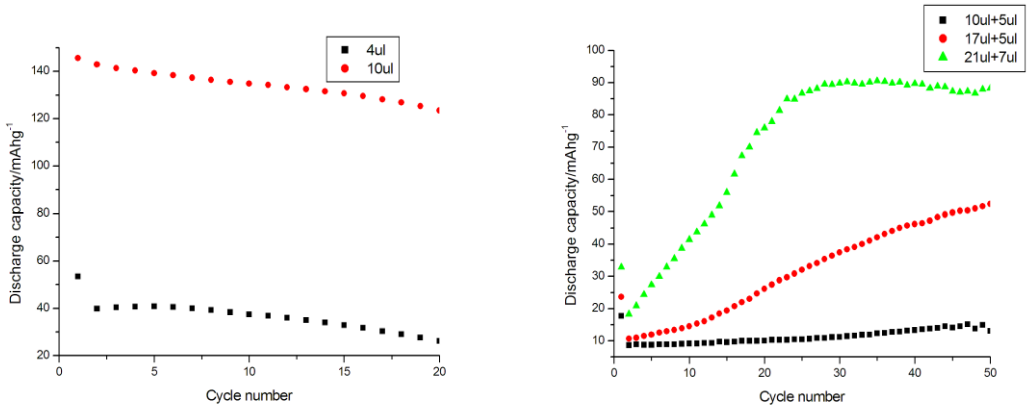

Figure 2.3 Left: discharge capacities for 4 µl and 10 µl electrolyte NCM523/Li half cells; Right: discharge capacities for different amounts of electrolyte in graphite/Li half cells

In graphite/Li half cells, for an active material mass loading of 10±0.5 mg, much more electrolyte is needed compared with NCM523/Li half cells. Since the porosity of graphite electrode is much larger than that of NCM523 electrode, more electrolyte is

needed to fill the pores and wet the active material. The comparison in discharge capacity is shown in **Figure 2.3**.

Normal 1st discharge capacity of graphite/Li half cell is 338 mAh/g. Even though three times amount of electrolyte (compared with NCM523/Li half cells) is added, the graphite electrode is not fully wetted and the discharge capacity is low (**Figure 2.3**).

The 3 wt% PEO modified coin cell showed no discharge capacity at 1C while it worked normally at C/10. The poor performance of PEO modified cell at high rate indicates the low conductivity of PEO. The results of nail penetration tests of charged reference and PEO-modified cells are shown in **Figure 2.4**.

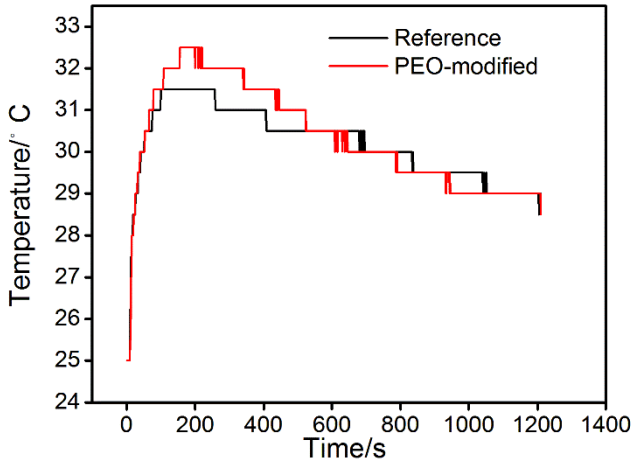

Figure 2.4 Nail test temperature profiles of reference and PEO-modified cells

The temperature profiles of reference and PEO-modified cells are similar, which indicates electrolyte absorbent may not reduce the temperature increase upon internal shorting. If an aggressive superabsorbent not only absorbs electrolyte but also swells in

the electrode, it might damage the contact between active material and conductive components, enhancing the thermal-runaway-mitigation efficiency.

2.3. Gas-Generation Agent

Upon a mechanical or thermal abuse, a gas-generation agent (GGA) could generate a large volume of gas, forming gas bubbles. The bubbles may block ion transport and displace electrolyte from the electrodes. The GGA under investigation was hydrazide compound. Hydrazide is widely used as blowing agent in plastic industry. It can be oxidized upon contact with charged cathode and generate gas. **Figure 2.5** shows a schematic of such a system.

Figure 2.5 Schematic of GGA working mechanism

2.3.1. Experimental

Xiamen Tob 140 mAh/g LIR-2450 cells (Li-ion rechargeable, diameter 24 mm, thickness 5 mm) were charged by constant current-constant voltage algorithm using a MTI BST8-WA battery analyzer to 4.3 V at C/5, with the cut-off current of C/50. The charged cells were disassembled and the electrode stacks together with the electrolyte were harvested in an Argon-filled glovebox (H_2O<0.5 ppm). Empty type-2450 cell cases

were modified by drilling two holes in the cathode-side shell; the holes were then covered with Kapton tapes. The harvested electrodes and electrolyte were re-assembled in the modified cell cases in the glovebox. The Kapton tapes were removed and two Tygon tubes were inserted into the holes and sealed with vacuum grease. Two thermocouples (Omega TT-K-40-25 type-K gauge 40) were respectively attached to the upper and bottom surfaces of the cell case, 7 mm away from the center and connected to a temperature logger (Omega OM-EL-USB-TC).

The cell was affixed to a polymethyl methacrylate (PMMA) holder and a steel nail was driven through the cell by a type-5582 Instron machine at the speed of 5 mm/s. After the nail fully penetrated the cell, the compression plate of the Instron machine moved back, leaving the nail inside the cell. The nail diameter was 3.4 mm. Immediately prior to the nail penetration, 200 μL 2-hydroxyethylhydrazine (2-HEH) was injected by a syringe into the modified cell through the Tygon tubing. In the reference test, the same amount of pristine electrolyte was injected into the cell.

2.3.2. Results and Discussion

The temperature profiles of reference and 2-HEH modified cells are similar, as shown in **Figure 2.6**.

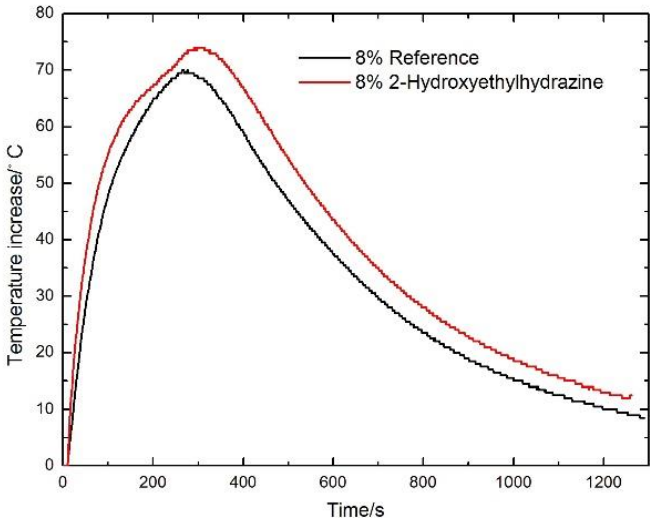

Figure 2.6 Nail test temperature profiles of reference and 2-HEH modified cells

2-HEH has no positive effect on the reduction of maximum temperature increase. When 2-HEH is dropped on cathodes, gas was generated vigorously. N-N bonds are oxidized by delithiated cathode and nitrogen gas is released. The reaction between hydrazide and charged cathode is an exothermal reaction and the heat generated would have an adverse effect on thermal runaway mitigation. While a non-conductive gas layer has beneficial effects on thermal runaway mitigation, the overall effect is dominated by the exothermic reactions.

2.4. Solvation Shell Interruption Agent

Lewis base have lone pairs of electrons, which would interrupt Li^+ solvation shells and influence the electrolyte conductivity. Dibenzylamine (DBA) could be dissolved in the electrolyte and therefore, was investigated as a TRR candidate. Simultaneous TRR

injection and nail penetration tests were performed, using a similar procedure as in Section 2.3.1. The temperature profiles of reference and DBA modified cells are shown in **Figure 2.7**. With 4% of DBA, the maximum temperature increase is reduced by a half. DBA is identified as a promising TRR candidate and will be further discussed in Chapter 3. In Chapter 4, an in-depth analysis of the working mechanism of DBA and other amines is presented.

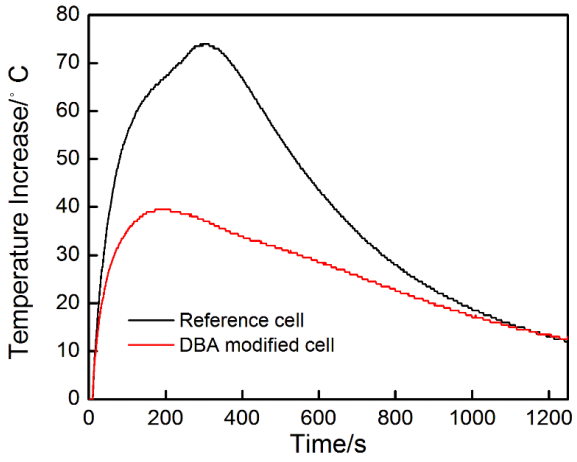

Figure 2.7 Nail test temperature profiles of reference and 4% DBA modified cell

2.5. Electrolyte-Displacement Agents

If a chemical could repel electrolyte and form a physical blocking layer between the cathode and anode, Li^+ transportation would be hindered. Since the electrolyte is hydrophilic, a hydrophobic chemical, octane is selected as a TRR candidate. Following a similar procedure as in Section 2.3.1, TRR injection and nail penetration tests were performed and the result is shown in **Figure 2.8**. The temperature profiles show that

octane is a promising TRR candidate. In Chapter 5, the working mechanism is investigated for octane and other alkanes with different chain lengths.

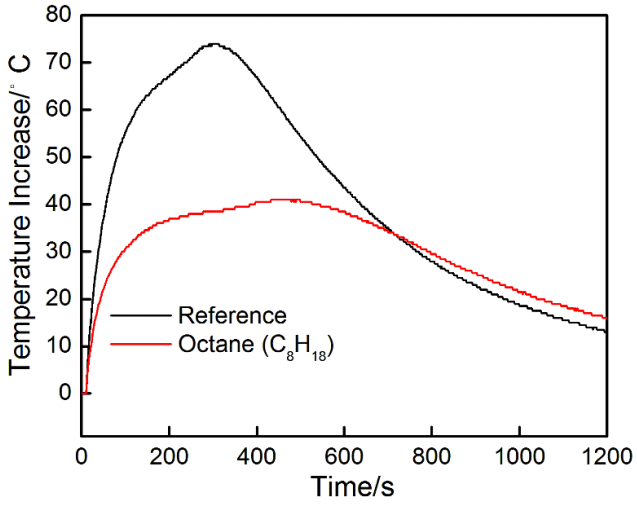

Figure 2.8 Nail test temperature profiles of reference and 4% octane modified cell

2.6. Conclusion

According to our experimental results, fire extinguishing agents, electrolyte superabsorbents, and gas-generation agents are less attractive TRR candidates, compared with solvation-shell interruption agents and electrolyte-displacement agents. A comprehensive study of the latter two classes of TRR candidates will be continued in Chapters 3-5.

Chapter 3. Mechanically Triggered Mechanism to Mitigate Thermal Runaway

In this chapter. a thermal-runaway retardant (TRR) of lithium-ion batteries (LIBs), dibenzylamine (DBA), is investigated. In a TRR-modified LIB, TRR is encapsulated in packages made of inert materials. When the LIB is subjected to mechanical abuse, the packages are broken apart and the TRR is released. In nail penetration and impact tests, addition of 4 wt% DBA reduces the temperature increase of fully charged LIR-2450 cells by nearly 50%. The influence of TRR packages on the cycling performance of LIBs is negligible. The working mechanism of DBA is associated with the decrease in electrolyte conductivity, the increase in charge transfer resistance, and the reduction in lithium ion (Li^+) transference numbers.

3.1. Introduction

Thermal runaway imposes major challenges to large-scale lithium-ion batteries (LIBs). The working temperature of a LIB is usually around room temperature [53]. Upon mechanical abuse such as an impact or nail penetration, the LIB cell components may fail and internal short circuits could be formed [54]. As a result, a series of exothermic electrochemical reactions and decompositions would take place and the local temperature can rapidly increase by 100-200 ˚C in less than one minute [55].

Great efforts have been made to enhance the safety of LIBs. A common approach to suppress thermal runaway is to embed thermally triggered safety components into LIBs,

such as trilayer separators that can close their pores when the internal temperature reaches the melting point of the middle layer, preventing further ion transport between electrodes [56-57]; low-melting-point microspheres that can cover the anode surface when they melt, preventing further ion disintercalation at the electrode-electrolyte interface [47]; positive-temperature-coefficient (PTC) layers that drastically increase the internal impedance at 110-150 °C [49, 58-60]; microcapsules that release fire extinguishing agents at 100-130 °C [61]; and thermally polymerizable monomers that thickens electrolyte [62]. One major issue of these thermal-runaway mitigation mechanisms is that they are activated only after the local temperature rises to above 90 °C, which is dangerously close to the acceleration point of the exothermic reactions [63]. Researchers have also investigated flame retardant additives (FRAs) [21, 64-67] that can reduce the electrolyte flammability, yet the battery performance is usually negatively affected [68]. Other approaches include electrode coating and doping that improve the thermal stability of the electrodes [69-75], but extensive fundamental study is still needed to enhance their efficacy and efficiency.

Mechanically triggered thermal-runaway mitigation mechanisms recently received increasing attention [76-78]. For instance, if a thermal-runaway retardant (TRR) is encapsulated in mechanically responsive packages made of materials inert within the battery environment, upon external mechanical loadings such as impacts or nail penetration the packages can be broken apart and release the TRR. This mechanism allows for the use of aggressive chemicals to suppress the short circuit discharge and the

subsequent exothermic phenomena, immediately after the battery is damaged, even before temperature increase begins. The main challenge is that the TRR must be highly efficient, such that it does not result in notable increase in cell mass or volume. In this work, we investigate dibenzylamine (DBA) as a TRR candidate. The influence of TRR-containing packages on the cycling performance of LIBs is also evaluated.

3.2. Experimental

3.2.1. Nail penetration test

Xiamen Tob 140 mAh/g LIR-2450 cells (Li-ion rechargeable, diameter 24 mm, thickness 5 mm) were charged by constant current-constant voltage algorithm using a MTI BST8-WA battery analyzer to 4.3 V at C/5, with the cut-off current of C/50. The charged cells were disassembled and the electrode stacks together with the electrolyte were harvested in an Argon-filled glovebox (H_2O<0.5 ppm). Empty type-2450 cell cases were modified by drilling two holes in the cathode-side shell and covered with Kapton tapes. The harvested electrodes and electrolyte were re-assembled in the modified cell cases in the glovebox. The Kapton tapes were removed and two Tygon tubes were inserted into the holes and sealed with vacuum grease. Two thermocouples (Omega TT-K-40-25 type-K gauge 40) were attached to the upper and bottom surfaces of the cell case respectively, 7 mm away from the center, and connected to a temperature logger (Omega

OM-EL-USB-TC).

The cell was affixed to a polymethyl methacrylate (PMMA) holder and a steel nail was driven through the cell by a type-5582 Instron machine at the speed of 5 mm/s. After the nail fully penetrated the cell, the compression plate of the Instron machine moved back, leaving the nail inside the cell. The nail diameter was 3.4 mm. Immediately prior to the nail penetration, 100 μL DBA (97%, Sigma Aldrich) was injected by a syringe into the modified cell through the Tygon tubing. In the reference test, the same amount of pristine electrolyte was injected into the cell.

To better understand the efficiency of DBA, nail penetration tests were also carried out on unmodified LIR-2450 cells at various states of charge (SOC). The unmodified LIR-2450 cells at various SOC were prepared by discharging fully charged (4.3 V) cells to cut-off discharge capacities of 35 mAh, 70 mAh, 105 mAh and 140 mAh, respectively.

3.2.2. Impact test

The LIR-2450 cells were charged to 4.3 V and the electrodes together with electrolyte were harvested through the same procedure as described in Section 3.2.1. Polyethylene/Aluminum/Polyester (PAP) trilayer (ULINE S-16893) was folded and heat sealed to form packages using an impulse sealer (Mcmaster-Carr), with 115 μL DBA or pristine electrolyte inside. The packages were first at rest in the glovebox vacuum antechamber for overnight to remove moisture, and then transferred into the glovebox for

the subsequent cell assembly. The harvested electrodes and electrolyte were re-assembled into an empty type-2450 cell case, with a DBA or electrolyte containing package sandwiched between the top cover and the electrode. The cells containing electrolyte packages were used as reference samples.

Impact tests on the re-assembled cells were performed using a table-top drop tower consisting of a stainless steel base and a polycarbonate track [76]. A stainless steel ball with the diameter of 6.35 mm was affixed at the center of the upper surface of the battery cell. A polyurethane cover guided a stainless steel rod; the diameter of the rod was 12.7 mm and the length was 50.8 mm [77-78]. The rod was placed on top of the steel ball. A cylindrical stainless steel hammer with the mass of 7.7 kg was dropped onto the rod. The drop distance was 18 cm. A type-K thermocouple was attached to the outer surface of the anode-side shell and the temperature was recorded in the same way as described in Section 3.2.1.

3.2.3. Measurement of cycling performance

Type-2016 coin cells were assembled to evaluate the influence of DBA-containing packages on the cycling performance. Cathode films were prepared by thoroughly mixing $LiNi_{0.5}Co_{0.2}Mn_{0.3}O_2$ (TODA America), polyvinylidene fluoride (Kynar 710), and carbon black (Timcal Super C65) powders with the mass ratio of 93:4:3. Slurries were produced in 1-Methyl-2-pyrrolidinone (Sigma Aldrich), cast on aluminum foil using a doctor blade,

and dried under vacuum at 80 °C for 24 hours. The electrode films had an active mass loading of about 6 mg/cm^2. Disk cathodes were cut, compressed using a rolling mill, dried again under vacuum for 4 hours, and transferred to an Argon-filled glovebox (H_2O < 0.1 ppm) for cell assembly. Small PAP packages containing ~5 μL DBA were sealed, vacuum-dried overnight, and attached to the inner surfaces of type-2016 cell cases using Kapton tapes. To assemble the cells, semi-circle pieces of the cathodes and lithium metal (Li) disk anodes were used. The electrolyte was 1 M $LiPF_6$ in ethylene carbonate and ethyl methyl carbonate (EC: EMC 1:1 wt%) and the separators were trilayer PP/PE/PP membranes (Celgard 2320). The coin cells were allowed to rest for 2 hours before the electrochemical tests were performed. Galvanostatic charge-discharge was carried out using a BST8-WA battery analyzer. The cells were charged and discharged at C/10 (1C = 200 mA g^{-1}) for the first cycle, followed by charging and discharging at 1C in the potential range of 3-4.3 V for all subsequent cycles. Reference cells with semi-circle cathodes and Li disks were also assembled and cycled without DBA-containing packages.

3.2.4. Interaction of DBA with electrodes

To understand the interaction between DBA and the electrodes, fully charged LIR 2450 cells were disassembled and the cathode and anode films were separated. About 100 μL DBA was dropped onto the harvested cathode or anode and the local temperature was recorded using the same thermocouple as in Section 3.2.1.

In addition, type-2016 coin cells were assembled in a similar way as in Section 2.2.3, without the PAP packages. The coin cells were allowed to rest for 2 hours and charged to 4.3 V at C/10. The charged cells were disassembled in the glovebox and the cathode disks were fully washed with dimethyl carbonate (DMC). The charged cathode disks were divided into two groups. The first group were soaked in 15 mL DBA for 20 min, followed by repeated rinsing with electrolyte and DMC. The washed cathode disks were re-assembled into coin cells with Li disks; the cells were discharged to 3 V at C/10 after resting for 2 hours. The second group were soaked in 100 μL DBA for 20 min. ^{1}H NMR spectra of DBA before and after the interaction with charged cathodes were recorded by a Varian Mercury Plus 400 MHz NMR spectrometer in $CDCl_3$. Mass spectra of DBA before and after the interaction with charged cathodes were obtained by a Thermo LCQdeca molecular mass spectrometer.

3.2.5. Interaction of DBA with electrolyte

The ionic conductivities of electrolytes containing different amounts of DBA (0-40 wt%) were measured by a conductivity meter (DDS 307A, Shanghai Yoke Instrument). Type-2016 coin cells were assembled through a similar procedure as in Section 2.2.4; the electrolyte was either pristine or modified with DBA. The coin cells were cycled at 1C after resting for 2 hours. Electrochemical impedance spectroscopy (EIS) measurements were carried out before and after cycling in the frequency range of 10^{6} Hz to 10^{-2} Hz with

the signal amplitude of 10 mV, using a Solartron Impedance/Gain-Phase Analyzer.

To measure the Li^+ transference numbers of pristine and DBA-modified electrolytes, Li metal symmetric cells were assembled. Type-2032 cell cases were used due to the increase in the thickness of cell components. Two Li metal disks were separated by a PP/PE/PP membrane, with a stainless steel spacer and a spring to ensure the tight contact between the components. The electrolytes under investigation were pristine reference (1 M $LiPF_6$ in EC: EMC 1:1 wt%) and 5 wt% DBA modified electrolyte. Potentiostatic polarization experiments were performed on the assembled coin cells with a constant voltage of 10 mV by an Arbin BT2000 battery testing system, until a steady-state current was reached. EIS measurements were carried out before and after the polarization.

3.3. Results and Discussion

Nail penetration creates a short circuit with consistent discharge dynamics. **Figure 3.1a** shows the experimental setup. The DBA amount is 4 wt% of the total mass of electrodes, current collectors, separator, and electrolyte. The measured temperature profiles of the two thermocouples attached to the top and bottom surfaces of the cells are similar, with a deviation of 1-2 ˚C. The temperature profiles measured from the top surface are used to show the characteristics of the system behaviors, which are displayed in **Figure 3.1b**. The addition of DBA reduces the temperature increase (ΔT_{max}) by about

50%, from ~75 ˚C in reference cells to ~40 ˚C in DBA-modified cells. The temperature ramp rates (**Figure 3.1c**) are calculated by differential analysis of the temperature profiles. Both reference and DBA-modified cells reach their maximum ramp rates (R_{max}) in about 8 s; DBA reduces R_{max} by ~30% from ~1 ˚C/m to ~0.7 ˚C/min.

A simplified model is used to estimate the generated heat over time, based on the following assumptions: (1) The temperature of the cell is isothermal and represented by the thermocouple measurement; (2) The convective heat transfer is considered and the radiative heat transfer is ignored [79]; and (3) the heat capacity of the added electrolyte or DBA is much smaller than that of the cell components. The heat generation rate (q') could be calculated by:

$$q' = (m_e C_{Pe} + m_s C_{Ps}) \frac{dT}{dt} + Ah(T - T_{amb}) \quad \textbf{(Eq. 3.1)}$$

where m indicates mass and C_P indicates specific heat; subscript "e" stands for the electrode stack containing electrolyte and subscript "s" stands for the stainless steel case together with the nail; T is the temperature of the cell and T_{amb} is ambient temperature; A is the surface area of the system that is exposed to air (including both the cell and nail) and h is the convective coefficient. The values of these parameters are given in Table 3.1. The total accumulated heat (q) is calculated by:

$$q = \int_0^t \left[(m_e C_{Pe} + m_s C_{Ps}) \frac{dT}{dt} + Ah(T - T_{amb}) \right] dt \quad \textbf{(Eq. 3.2)}$$

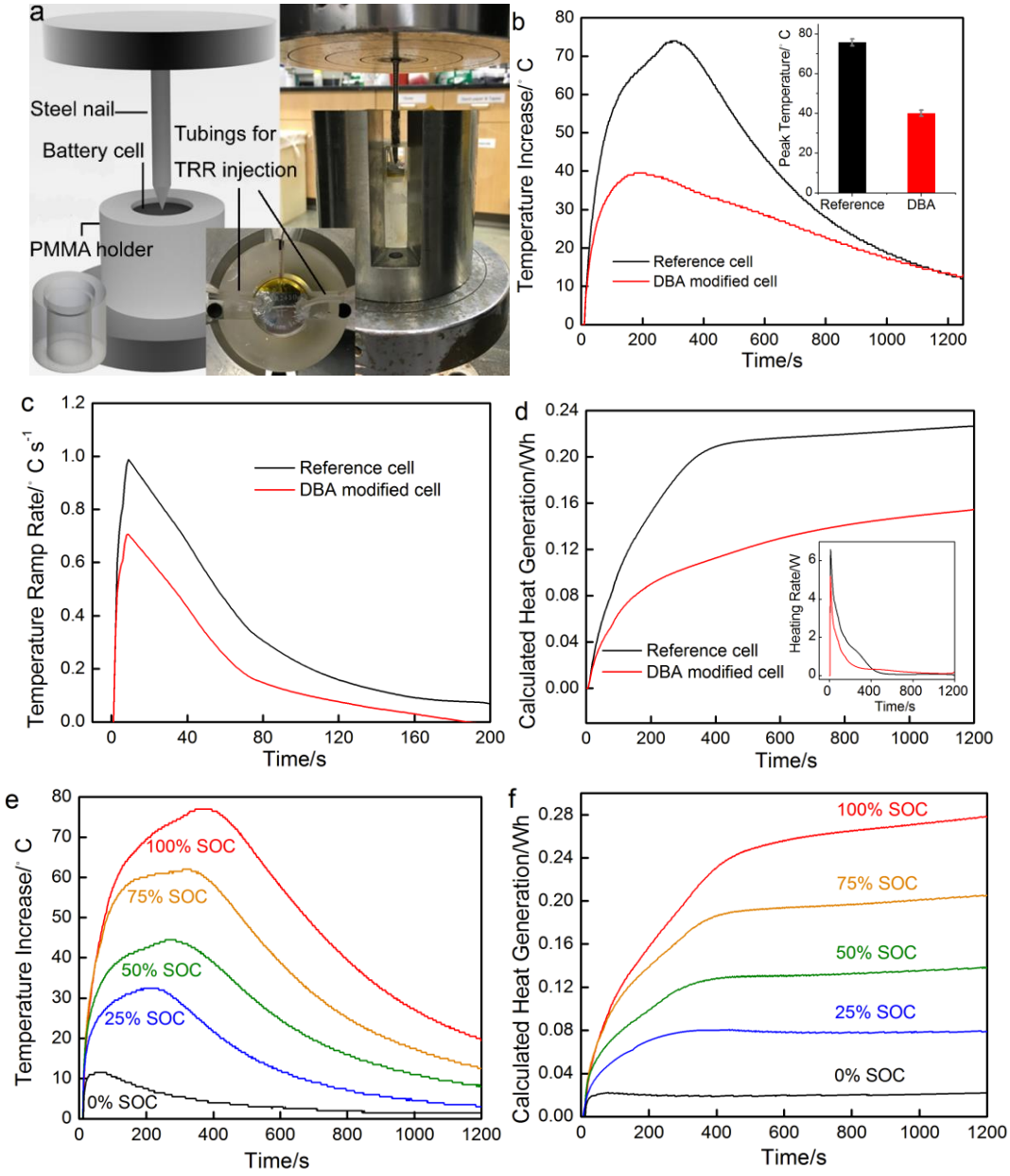

Figure 3.1 (a) The nail penetration test setup; the left bottom inset shows the shape of the PMMA holder; the middle inset shows the top view of a coin cell. (b) Typical temperature profiles of nail penetration tests on the reference and the DBA-modified cells; the inset shows the peak temperatures with error bars. (c) The temperature ramp rates in the first 200 sec. in nail penetration tests. (d) Generated heat of the reference and the DBA-modified cells, calculated from Eq. 3.2; the inset shows the heating rate. (e) Typical temperature profiles and (f) the generated heat of the reference LIR-2450 cells at various SOC.

Table 3.1 The parameters used in Equations (1) and (2)

m_e (kg)	m_s (kg)	C_{Pe} (J/kg K)	C_{Ps} (J/kg K)	A (m^2)	h (W/m^2 K)
2.2×10^{-3}	7.2×10^{-3}	1100 [80]	500	1.8873×10^{-3}	7.9 [81]

Figure 3.1d shows the generated heat of reference and DBA-modified cells, obtained from Eq. 2.2; the inset shows the heat generation rate obtained from **Eq. 3.1**. The heat generation in the first 20 min is 0.23 Wh for the reference cell and 0.15 Wh for the DBA-modified cell, respectively. The addition of 4 wt% DBA leads to about 1/3 reduction in generated heat during the time period of measurement. Eventually the DBA-modified cell should generate about the same amount of heat as the reference cell, but it takes quite a long time and may not be particularly critical to thermal runaway mitigation, since the peak temperature is almost always reached in the first few minutes.

Figure 3.1e shows typical nail penetration temperature profiles of unmodified LIR-2450 cells at different SOC. The heat generation is analyzed by **Eq. 3.2** and the result is displayed in **Figure 3.1f**. Compared with the peak temperatures of the modified reference cell (**Figure 3.1b**), ΔT_{max} of a fully charged unmodified cell is slight higher and the post-peak temperature decrease rate is somewhat lower, which may be attributed to the resistance increase during reassembly. By adding 4 wt% DBA, the temperature profile of a fully charged cell is similar to that of the reference cell at 50% SOC; that is, nearly 50% of the stored electricity cannot be converted to thermal energy.

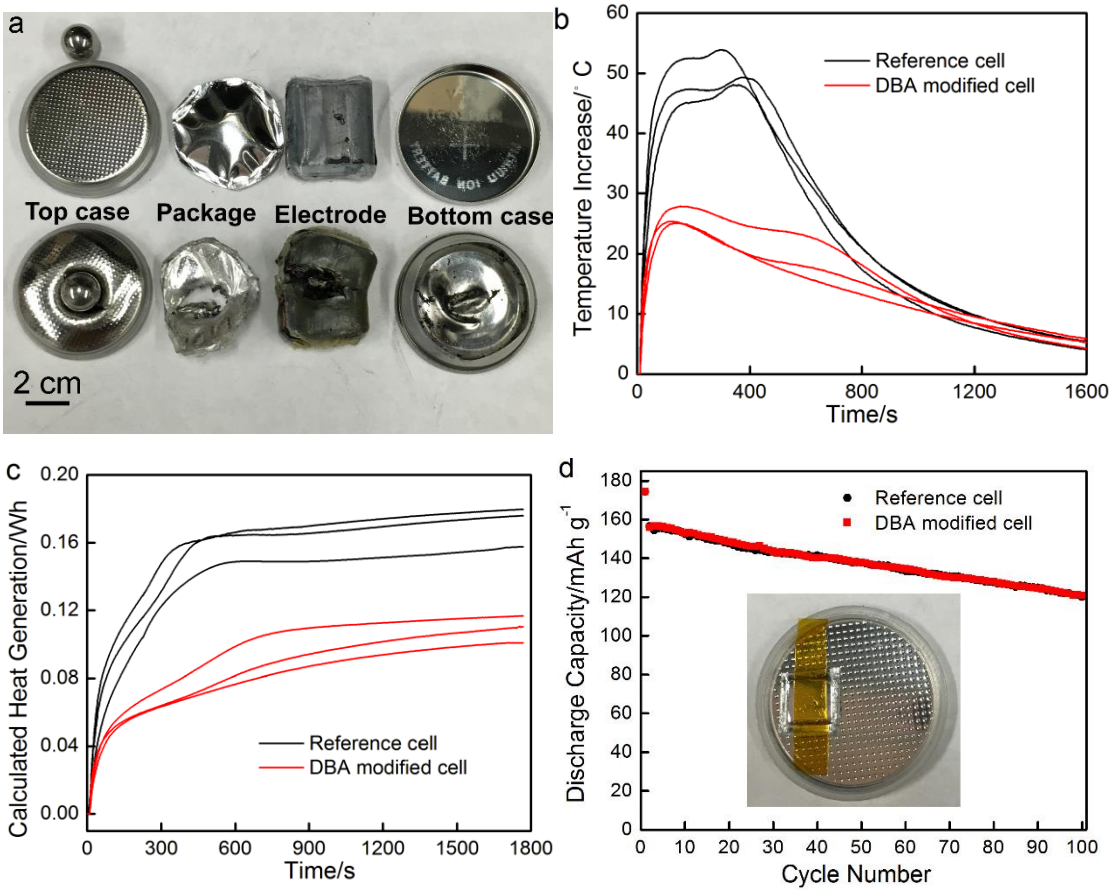

Figure 3.2 (a) Cell components before (top) and after (bottom) the impact. (b) Temperature profiles of six LIR-2450 cells embedded with TRR packages. (c) Calculated heat generation of the six LIR-2450 cells. (d) Cycling performance of coin cells with embedded TRR packages; the inset is a photo of a modified coin cell

The impact test on LIR-2450 cells with embedded TRR-containing packages confirms that the TRR could be sealed under working condition and be released as the cell is damaged. The DBA amount is 5 wt% of the total mass of electrodes, current collectors, separator, and electrolyte. **Figure 3.2a** displays the cell components before assembly and after impact. The TRR package is broken apart upon impact. The temperature profiles of reference and DBA-modified cells are shown in **Figure 3.2b**; each

group contains three cell samples. The heat generation shown in **Figure 3.2c** is calculated through **Eq. 3.2**. It can be seen that for all the samples ΔT_{max} in impact test is smaller than that in nail penetration test, because the nail penetration leads to a more intense internal shorting. In impact test, DBA decreased ΔT_{max} by about 50%, similar to the nail penetration test.

The TRR package is made from the PAP trilayer material, because: (1) the polyethylene can be conveniently heat sealed; (2) the dense aluminum middle layer offers an ultra-low permeability; and (3) the outer polyester layer insulates the aluminum layer. **Figure 3.2d** shows the cycling performance of coin cells with DBA-containing packages. The packages have little influence on the cell capacity up to 100 cycles.

To investigate the working mechanism of DBA, the interaction of DBA with electrodes is studied. As DBA is dropped on the cathode and anode harvested from a fully charged (4.3 V) LIR-2450 cell, local temperature is monitored continuously. Upon exposure to DBA, a sudden temperature increase is observed on the charged cathode, yet the temperature of anode remains nearly constant (**Figure 3.3a**), indicating that a DBA-cathode interaction takes place. Charged cathode disks are then soaked up in DBA. After the cathodes are thoroughly washed to remove remaining DBA, they are reassembled into coin cells with pristine electrolyte. The specific discharge capacities of the two types of reassembled cells are 164 mAh/g and 149.2 mAh/g respectively (**Figure 3.3b**). For the reassembled reference cell, the initial voltage drop is due to the voltage relaxation. The

voltage drop of the cell containing DBA-treated cathode is larger than that of the reference cell. In a parallel test, excess charged cathode materials were allowed to react with DBA in order to determine the reaction products, but no change is observed in the ^{1}H NMR spectra and mass spectra of DBA before and after the reaction, suggesting that the reaction products of DBA are not in liquid phase. Moreover, no gas generation is observed during the reaction of DBA with the charged cathode. It is possible that a solid layer of reaction product is deposited on the cathode surface. The initial voltage drop and the capacity loss might be attributed to this additional resistive layer. Note that the DBA-treated cathode could still deliver 91% of the discharge capacity of the reference cathode, and the fact that DBA-cathode reaction is exothermic (**Figure 3.3a**) is against the observed reduction in ΔT_{max}. Therefore, the chemical reactions between the cathode and DBA should not be a major factor that influences the heat generation in nail penetration and impact tests.

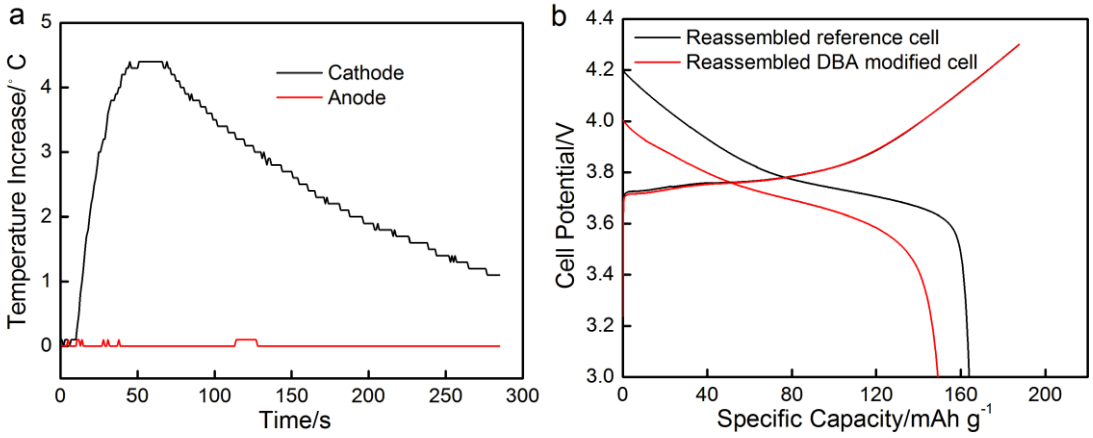

Figure 3.3 (a) Typical temperature profiles of cathode and anode exposed to DBA. (b) Typical Charge-discharge curves of the reassembled reference and DBA-modified cells at C/10

The effects of DBA addition on the electrolyte are investigated. As shown in **Figure 3.4a**, the ionic conductivity of pristine electrolyte is 9.23 mS/cm. The 5 wt% and 10 wt% DBA-modified electrolytes have reduced ionic conductivity of 7.59 mS/cm and 6.38 mS/cm, respectively. Coin cells assembled with pristine electrolyte as well as 5 wt% or 10 wt% DBA containing electrolyte are cycled at 1C and the cell potentials dynamics over time are shown in **Figure 3.4b**. The cell with 5 wt% DBA has a larger polarization and a greatly reduced capacity compared to the reference cell; the cell with 10 wt% DBA has the lowest capacity and cannot be normally charged and discharged. Clearly, DBA significantly increases the cell impedance. EIS measurements are performed on the cells before and after 5 charge-discharge cycles. **Figure 3.4c** and **Figure 3.4d** show the Nyquist plots, equivalent circuits, and fitted curves, with R_s being the electrolyte resistance, R_{sei} the solid electrolyte interface (SEI) resistance, and R_{ct} the charge-transfer resistance [82]. **Table 3.2** shows the resistance values according to the fitting results from the equivalent circuit. Clearly, the DBA-modified cell has not only a larger electrolyte resistance, but also much higher SEI and charge-transfer resistances.

Table 3.2 Resistance values of equivalent circuits in EIS measurement

	After assembly		After 5 cycles		
	R_s (Ω)	R_{ct} (Ω)	R_s (Ω)	R_{sei} (Ω)	R_{ct} (Ω)
Reference cell	50	250	58	254	450
DBA-modified cell	75	1050	65	1040	1700

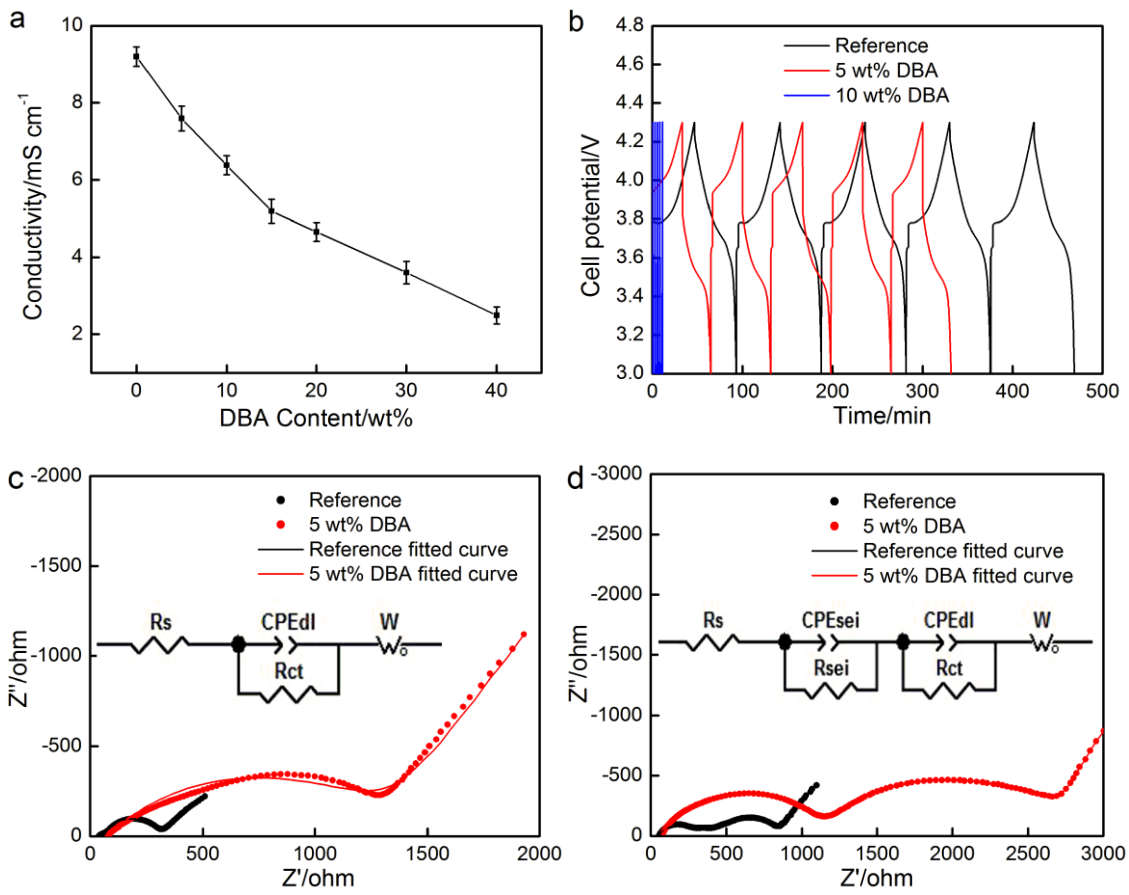

Figure 3.4 (a) Ionic conductivity of the DBA-modified electrolyte. (b) Typical voltage profiles of the reference and DBA-modified cells. Nyquist plots, equivalent circuits, and fitting plots: (c) immediately after reassembly and (d) after 5 charge-discharge cycles.

The effect of DBA addition on the Li^+ transport property is further investigated through the measurement of Li^+ transference numbers by a potentiostatic polarization method [83-84], in which a constant voltage of 10 mV (ΔV) is applied on a Li metal symmetric cell. During the polarization, the current drops from the initial value (I_0) to a steady-state value (I_{ss}). **Figure 3.5a** and **Figure 3.5b** display the current drop with time, and the insets show the Nyquist plots from EIS measurements before and after polarization. In the

corresponding equivalent circuit, R_1 and R_2 are the Li-electrolyte interfacial resistances, and R_e is the electrolyte resistance [84-85]. The Li^+ transference numbers t_{Li}^+ is given by [86]:

$$t_{Li^+} = \frac{I_{ss}}{I_0}\left(\frac{\Delta V - I_0 R_0}{\Delta V - I_{ss} R_{ss}}\right) \quad \textbf{(Eq. 3.3)}$$

where R_0 and R_s equal to the sum of R_1 and R_2 before and after polarization, respectively. **Table 3.3** shows the values of I_0 and I_{ss} during polarization, the resistance values from the fitting results, and the calculated Li^+ transference numbers of reference and DBA-modified electrolyte. The Li^+ transference numbers of reference electrolyte is 0.48, which is consistent with the data in open literature [87]. The addition of 5 wt% DBA decreases the Li^+ transference number to 0.23.

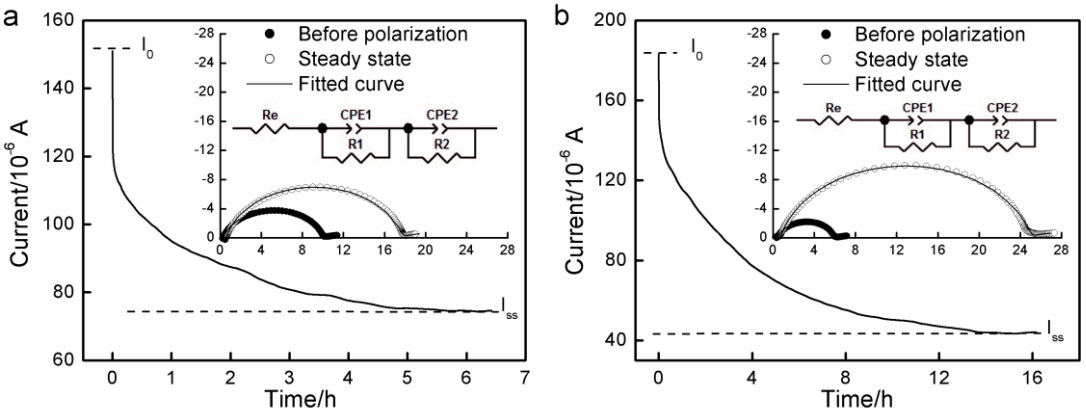

Figure 3.5 Polarization curves of Li metal symmetric cells with (a) pristine electrolyte and (b) electrolyte containing 5 wt% DBA; the insets show the Nyquist plots before and after polarization.

Table 3.3 The measurement results of Li^+ transference numbers

	I_0	I_{ss}	Re_0	Re_{ss}	R_0	R_{ss}	t_{Li}^+
Reference cell	151.102	74.454	0.271	0.548	12.345	22.032	0.48
DBA-modified cell	183.487	43.687	0.402	0.715	8.304	28.218	0.23

The testing data show that the addition of DBA increases the electrolyte resistance and the charge transfer resistance, and decreases the Li^+ transference number, all of which would suppress the Li^+ transportation. Clearly, the modification of electrolyte is a major reason of the hindered heat generation and the reduced ΔT_{max} in nail penetration and impact testing. The increased resistances and reduced Li^+ transference number may result from the Lewis base characteristic of DBA. Previous studies reported that adding Lewis acid to an electrolyte could improve the conductivity by forming complex with salt anions [88]. The Lewis acid serves as an anion receptor, enhances the dissociation of ion pairs, and increases the population of free cations [89]. The dissociation of ion pairs contributes to a high Li^+ transference number. DBA is a Lewis base and an electron donor, which may repel the $PF6^-$ anions and decrease the dissociation of Li^+ solvation shell and $PF6^-$ pairs, resulting in the decrease in Li^+ transference number and conductivity.

The current study on coin cells demonstrate the concept of including DBA packages in battery cells. The conditions in large-sized pouch cells are different from coin cells, in terms of cell size, mass, electrolyte-electrode mass ratio, etc. The study on pouch cells is an important topic of our future study.

3.4. Conclusions

Dibenzylamine (DBA) is identified as a promising thermal runaway retardant of lithium-ion batteries. Upon nail penetration or impact, the temperature increase of a fully charged LIR-2450 cell with 4 wt% DBA could be reduced by ~50%. Embedding DBA-containing packages in coin cells does not affect the cell capacity and the cycling performance up to 100 cycles. Charged anode does not react with DBA. Exothermic reactions between DBA and charged cathode are observed, but it is not a governing factor of the reduced heat generation of damaged cells. The major working mechanism of DBA is associated with the increase in electrolyte and charge transfer resistances as well as the decrease in Li^+ transference numbers.

3.5. Acknowledgements

Chapter 3, in full, is a reprint of the material "Exothermic behaviors of mechanically abused lithium-ion batteries with dibenzylamine" as it appears in the Journal of Power Sources, Yang Shi, Daniel J. Noelle, Meng Wang, Anh V. Le, Hyojung Yoon, Minghao Zhang, Ying Shirley Meng, Yu Qiao, 2016, 326, 514-521. The dissertation author was the first author of this paper and conducted all the essential research work.

Chapter 4. Roles of Amines in Thermal-Runaway-Mitigating Lithium-Ion Battery

Benzylamine (BA), dibenzylamine (DBA), and trihexylamine (THA) are investigated as thermal runaway retardants (TRR) for lithium-ion batteries (LIBs). In LIBs, TRR is packaged separately and released only when internal shorting happens, so as to suppress exothermic reactions and slow down temperature increase. THA is identified as the most efficient TRR. Upon nail penetration, 4 wt% THA can reduce the temperature increase by nearly 50%. It is discovered that the dominant working mechanisms of the three investigated amines are different: THA is highly wettable to separators and is immiscible with electrolyte, and therefore blocks lithium ion (Li^+) transport; BA and DBA decrease the ionic conductivity of electrolyte and increase the charge transfer resistance. All the three amines react with charged electrodes; the reactions of DBA and THA do not have much influence on the overall heat generation, while the reaction of BA cannot be ignored.

4.1. Introduction

Because of their high specific energy and excellent cost-performance balance, lithium-ion batteries (LIBs) are promising candidates to large-scale energy storage systems such as battery packs in smart grids and electric vehicles. [90-91] While LIBs are generally safe and generates little heat during normal operation, once a single LIB cell is damaged, thermal runaway may happen and seriously threaten the entire structure. [54]

Currently, LIB robustness remains a major concern in energy storage system design.

As a LIB cell is largely deformed, its components may be broken apart, leading to the direct contact between cathode and anode and a large internal shorting current (ISC). The immense amount of energy stored in the LIBs can be released in a short period of time, accompanied by a rapid temperature rise. Once the local temperature is beyond 90-100 ◦C, a series of reactions among electrolyte, electrodes, and solid-electrolyte interface (SEI) layers are accelerated. [55] The electrolytes used in today's and near-future LIBs are highly volatile and flammable. [67] If they are ignited, catastrophic system failure would happen.

For a couple of decades, researchers have investigated a number of active thermal-runaway mitigation (TRM) techniques; most of the TRM mechanisms were thermally triggered. For instance, electrodes may be modified by positive temperature coefficient (PTC) materials [49, 58-60] or low-melting-point microspheres. [47] At 100-130 °C, the TRM additives greatly increase the internal impedance and therefore, ISC is reduced and the heat generation becomes slower. A major issue is that, once the temperature is higher than 110 ◦C, the temperature ramp rate increases drastically, and the thermally activated processes may not be sufficiently fast to guarantee a satisfactory safety.

Recently, we developed mechanically triggered methods [76-77, 92] by embedding thermal runaway retardant (TRR) packages in LIBs. [93] Upon mechanical abuse of the LIBs, TRR packages are broken apart and release TRR, which mitigates thermal runaway.

A schematic is shown in **Figure 4.1a**. The main challenge comes from the efficiency of TRR: TRR must suppress the exothermic reactions without any sacrifice in battery capacity or large increase in mass and volume of the system. In our previous work we identified dibenzylamine (DBA) as an efficient TRR candidate. [93] In this study, its primary amine counterpart, benzylamine (BA) and a tertiary amine, trihexylamine (THA), are investigated to understand the working mechanisms of amines. It is discovered that THA is more efficient than DBA. The chemical structures of BA, DBA and THA are depicted in **Figure 4.1b**.

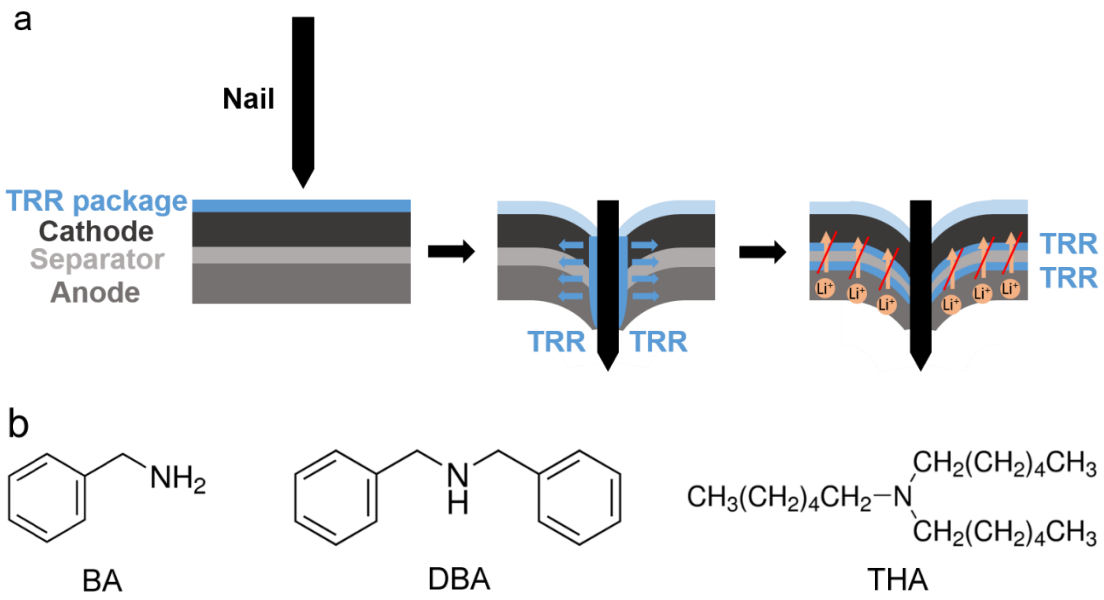

Figure 4.1 (a) Schematic of using TRR to mitigate thermal runaway: Left - During normal operation, TRR is sealed in a separate package; Middle - As the cell is damaged, the package ruptures and TRR is released; Right - TRR suppresses the Li^+ transport and heat generation associated with internal shorting. (b) Chemical structures of BA, DBA and THA.

4.2. Experimental Section

4.2.1. Nail penetration test

Nail penetration tests were conducted, following the procedure described in our previous work. [93] LIR-2450 cells were first fully charged to 4.3 V, and then disassembled and re-assembled with open cell cases. The open cases contained two holes, which allowed for the injection of TRR. 100 μL amine (BA, DBA or THA) or pristine electrolyte was injected through the holes. The pristine electrolyte contained 1 M LiPF6 in ethylene carbonate (EC) and ethyl methyl carbonate (EMC), with the EC to EMC mass ratio of 1:1, and was employed as the reference additive. Immediately after the injection, a steel nail penetrated through the cell, causing internal shorting and heating. Details of the testing procedure are similar to that of our previous work. The temperature of the cell was recorded by a thermocouple and the distance between the nail and the tip of thermocouple was around 7 mm.

4.2.2. Properties of amine-modified electrolyte

Wettability tests and contact angle measurements (KSV Instruments CAM 100) were carried out by dropping 50 μL electrolyte or amines on trilayer PP/PE/PP separators (Celgard 2320). The conductivities of the electrolytes with various BA or DBA concentrations were recorded by a conductivity meter.

To evaluate the influence of amines on cell resistance, 2016 coin cells were made following the procedure established previously. [93] Cathode was composed of $LiNi_{0.5}Co_{0.2}Mn_{0.3}O_2$, carbon black, and polyvinylidene fluoride, with the mass ratio of 93:3:4. The cells were assembled with lithium disks as anodes, and PP/PE/PP membranes as separators. Electrochemical impedance spectroscopy (EIS) measurements were carried out on the cells assembled with pristine electrolyte (1M $LiPF_6$ in EC:EMC 1:1) and electrolyte containing 5 wt% BA or DBA.

High-performance liquid chromatography (HPLC) analysis was performed on a Jupiter Proteo90A Phenomenex Column (150 × 4.60 mm) using a Hitachi-Elite LaChrome L-2130 Pump equipped with a UV-Vis Detector (Hitachi-Elite LaChrome L-2420). Buffer A was 0.1% trifluoroacetic acid (TFA) in water and Buffer B was 99.9% acetonitrile (ACN) and 0.1 % TFA. Mass spectra of products from HPLC were recorded by Thermo LCQdeca. Fourier transform infrared spectroscopy (FTIR) measurements were performed using Bruker ALPHA FTIR Spectrometer from 4000 to 450 cm^{-1}. The experimental backgrounds were corrected by using the OPUS software package. FTIR analysis of the mixtures of EC-EMC solvent modified by different amount of BA or DBA was carried out after the components were homogenized by magnetic stirring for 30 mins. 0.1 g $LiPF_6$ had been added to 1 mL BA or DBA, followed by 30 min magnetic stirring and passing through a 200-nm pore-size PTFE filter to remove undissolved $LiPF_6$. FTIR analysis of the filtered solution was then performed.

4.2.3. Interaction of amines with electrodes

To understand the interaction between amines and electrodes, cathode and anode films were separately harvested from fully charged LIR 2450 cells. 100 μL amime (BA, DBA or THA) was dropped onto the electrodes and the local temperature was measured.

2016 coin cells were made according to the procedure in Section 2.2 and charged to 4.3 V at 20 mA g^{-1} after resting for 2 hours. The cathode disks from disassembled charged cells were rinsed with dimethyl carbonate (DMC) in the glovebox, and divided into three groups. The first group of cathode disks were soaked in 15 mL selected amine for 20 min, followed by thorough rinsing with DMC. New coin cells were made with the rinsed cathodes and lithium disk anodes; the cells were discharged to 3 V at C/10 after resting for 2 hours. The second group of cathode disks were also soaked in selected amines, followed by thorough rinsing, and then analyzed using X-ray Photoelectron Spectroscopy (XPS) (Kratos AXIS Supra) with Al K_α radiation. All the spectra were calibrated by assigning the C 1s peak at 284.6 eV. For the third group, 50 mg charged cathode disks were soaked in 0.5 mL BA, DBA or THA for 20 min and then mass spectra of the amine phases were recorded by a the same mass spectrometer to detect the reaction products.

4.3. Results and Discussion

The amine injection immediately before the nail penetration simulates the working

process of TRR: During normal operation of a LIB cell, TRR is sealed in non-permeable packages inside the cell case, separated from electrodes and electrolyte [93]; when the cell is damaged, TRR packages rupture and TRR is released into the cell, simultaneously as internal shorting takes place. In the current research, the TRR amount is kept as 4 wt% of the total weight of cathode, anode, electrolyte and separator.

Figure 4.2a shows the temperature profiles of the cells under the influence of TRR. Among the three amines, BA has the least effect on maximum temperature increase (ΔT_{max}); THA is the most efficient one to reduce ΔT_{max}, better than DBA which was investigated previously. [93] Addition of THA reduces ΔT_{max} by about 50%, from ~75 ˚C in reference cells to ~36 ˚C. **Figure 4.2b** shows the calculated heat generation in the first 20 minutes after nail penetration, using an analytical model that accounts for convective heat transfer, with radiative heat transfer being ignored. [93] 4 wt% THA results in about 45% reduction in heat generation, from ~0.23 Wh in reference cells to ~0.13 Wh.

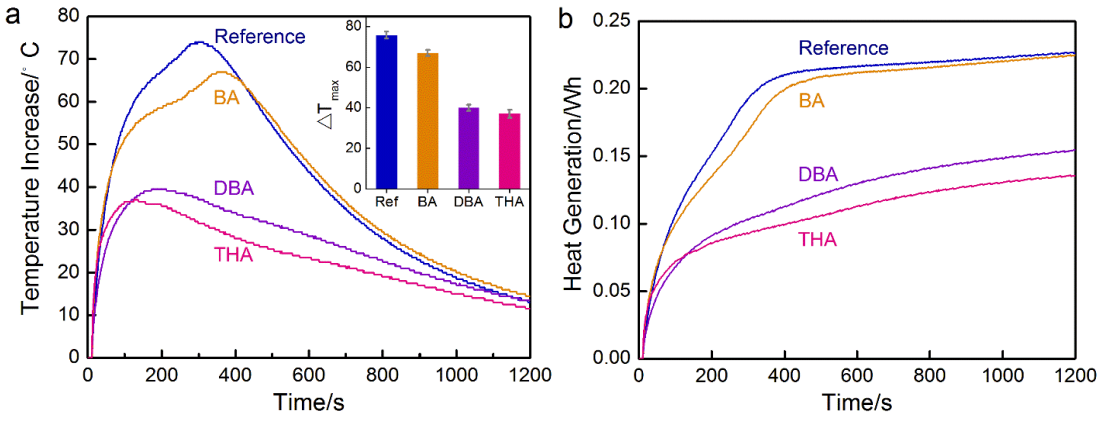

Figure 4.2 (a) Nail penetration test temperature profiles on the reference and amine-modified cells; the inset shows the maximum temperatures increase. (b) Calculated heat generation of the reference and amine-modified batteries

The three amines under investigation, namely BA, DBA, and THA, represent primary, secondary, and tertiary amines, respectively. They have different effects on ΔT_{max}, which should be related to both of their physical and chemical properties. BA and DBA are miscible with electrolyte while THA is not; the latter enables THA to form a blocking layer between cathode and anode, using the porous separator as the scaffold. Wettability tests results (**Figure 4.3a**) indicate that in a given period of time, THA can spread over a much larger area on separator than electrolyte, BA, and DBA. The contact angle measurement further confirms that THA is by far the most wettable liquid to the separator (**Figure 4.3b**). Thus, when THA is released into the LIBs, it rapidly disperses in the separator and displaces the electrolyte in the separator pores, forming a physical barrier layer between the electrodes such that Li^+ transport is suppressed. As the internal impedance largely rises, ISC decreases, so does the heat generation.

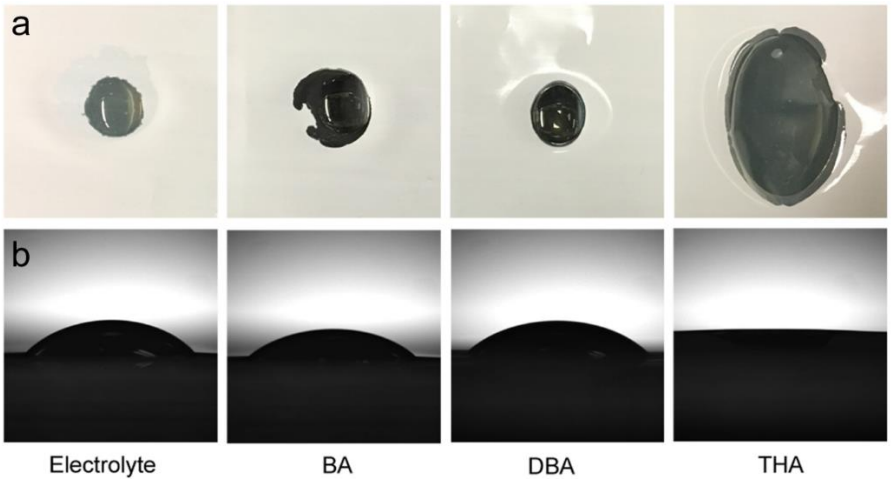

Figure 4.3 (a) Top view of wettability tests and (b) side view of contact angle measurement of electrolyte and amines.

Both BA and DBA are miscible with the electrolyte and therefore, cannot physically block ion transport; however, they do reduce the ionic conductivities of the electrolyte. As shown in Figure 3.4a, when more BA or DBA is added, the electrolyte conductivity decreases monotonously. With the same amount of amine, DBA can reduce the electrolyte conductivity more efficiently than BA. **Figure 4.4b** displays the EIS measurement results of the coin cells assembled with pristine and BA or DBA modified electrolytes, in which Rs is the electrolyte resistance and Rct is the charge transfer resistance. [82] **Table 4.1** shows the resistance values extracted from the fitting results. While the BA-modified cell has a lower electrolyte resistance, it has a larger charge transfer resistance than the DBA modified cell.

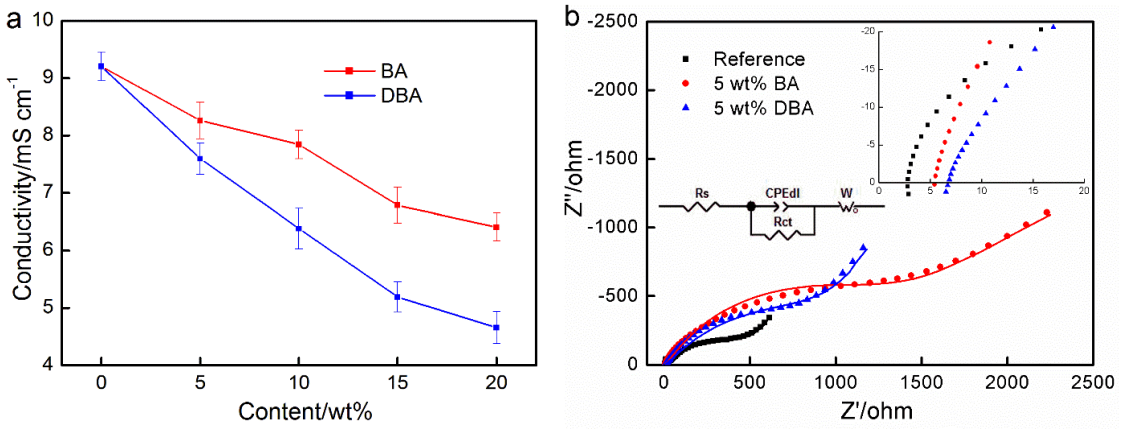

Figure 4.4 (a) Ionic conductivity of BA and DBA modified electrolytes. (b) EIS measurement results of reference, BA-modified, and DBA-modified cells; the inset displays the plots at an enlarged scale

Table 4.1 Resistance values in EIS measurement

	Reference (Ω)	BA (Ω)	DBA (Ω)
R_s	2.81	5.43	6.76
R_{ct}	395	997	802

The reduction in conductivity of BA or DBA modified electrolyte may be caused by the influence of amine on either the solvent (EC and EMC) or the solute ($LiPF_6$), or both. Amines may attack the carbonyl carbon in EC, followed by ring-opening that gives a urethane product. [94] BA-EC and DBA-EC reactions are proposed, as displayed in **Figure 4.5a** and **Figure 4.5b**. HPLC is used to separate the possible reaction products between the amines and the electrolyte solvent; it shows that both BA and DBA react with EC while neither of them reacts with EMC. The mass spectra results show that the molecular weights of BA-EC and DBA-EC reaction products are as expected in **Figure 4.5a** and **Figure 4.5b**, which confirms the proposed reaction mechanism. FTIR measurements are carried out to demonstrate the BA-EC and DBA-EC reactions. **Figure 4.6a** shows the FTIR spectra of pure BA, EC-EMC solution, and their mixtures. The bands corresponding to the C=O stretching vibration mode of the EC molecule are observed at 1774 cm^{-1} and 1799 cm^{-1}, in which the 1774 cm^{-1} band is attributed to the C=O stretching and the 1799 cm^{-1} band to the overtone of the ring breathing mode. [95] The 1743 cm^{-1} band is attributed to the C=O stretching vibration mode of the EMC molecule. [95] As BA is added to the EC-EMC solution, the bands at 1774 cm^{-1} and 1799 cm^{-1} become weaker and a new band at 1707 cm^{-1} shows up. The new band is attributed to the urethane carbonyl group. [96] With the increasing amount of BA, the carbonate absorption bands (1774 cm^{-1} and 1799 cm^{-1}) disappear and are replaced by the urethane carbonyl band. **Figure 4.6b** shows the FTIR

spectra of pure DBA, EC-EMC solution, and their mixtures. Compared with **Figure 4.6a**, as DBA is added to the EC-EMC solution, the C=O stretching mode of EC does not disappear and no new band is observed. This is due to the small amount of EC-DBA reaction products, which is consistent with the HPLC analysis. Clearly, according to the HPLC analysis and the FTIR spectra, BA-EC reaction is more aggressive than the DBA-EC reaction.

When BA and electrolyte is mixed, white precipitates gradually appear, accompanied by heat generation, which should be associated with the $LiPF_6$-catalyzed exothermic polymerization of EC. [97] The reaction mechanism is displayed in **Figure 4.5c**. Such phenomena are not observed in the DBA-electrolyte mixture.

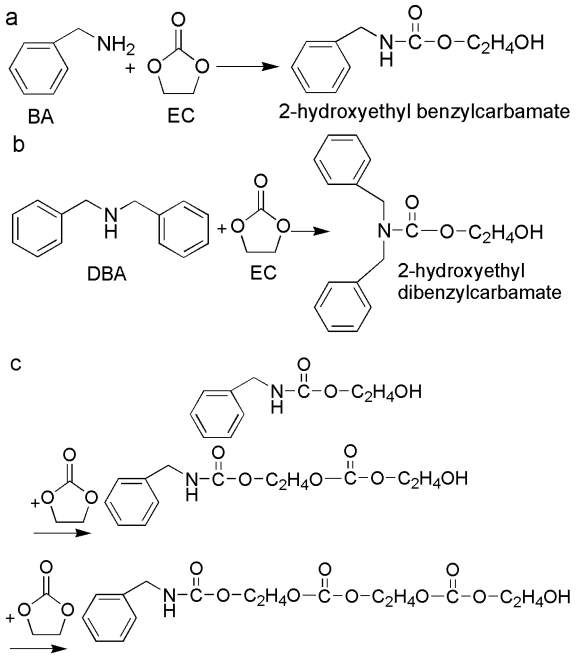

Figure 4.5 Proposed reaction mechanisms of (a) BA and EC, (b) DBA and EC, and (c) $LiPF_6$ catalyzed EC polymerization.

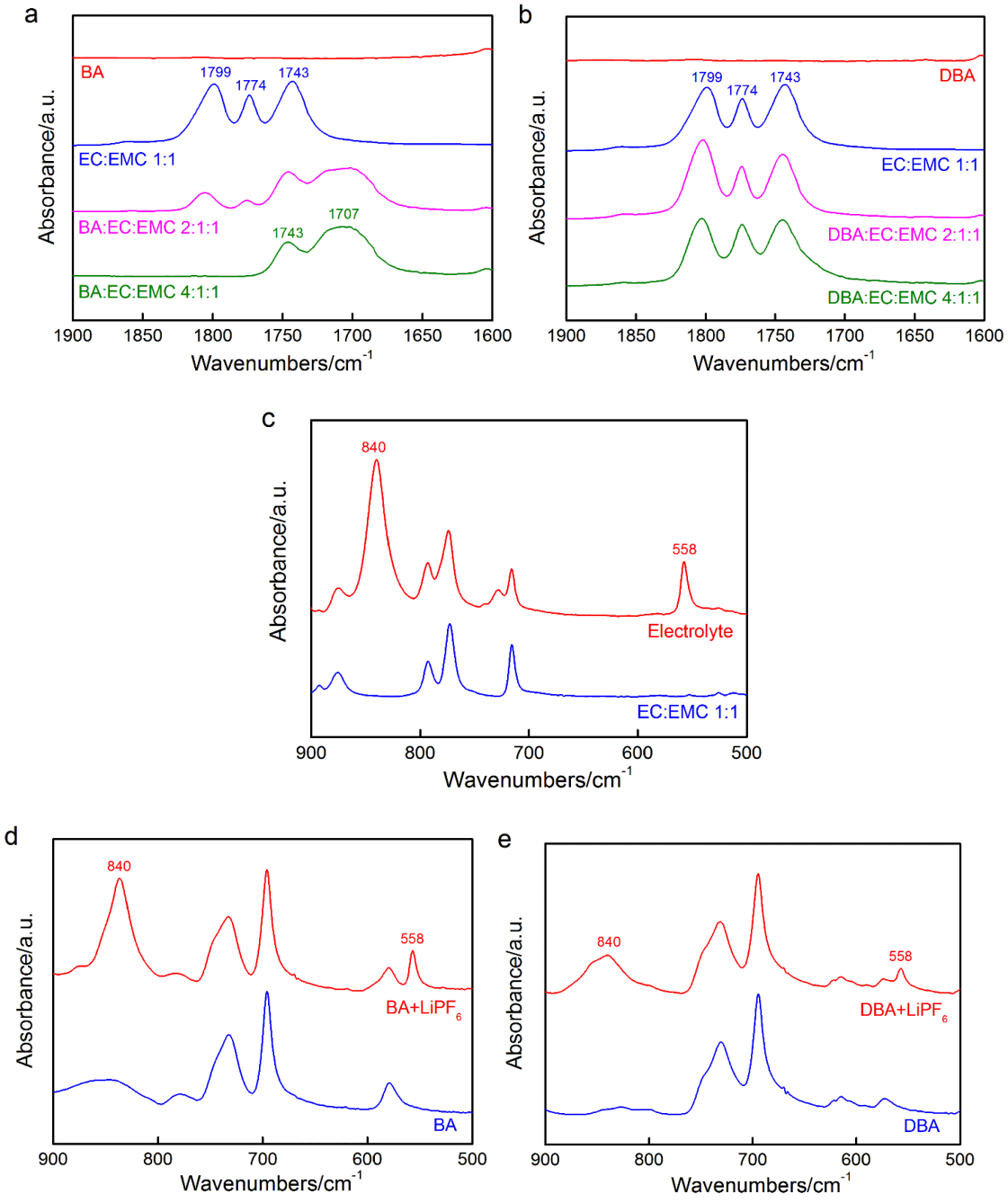

Figure 4.6 FTIR spectra of (a) BA, EC-EMC solvent, and their mixtures; (b) DBA, EC-EMC solvent, and their mixtures; (c) electrolyte and EC-EMC solvent; (d) BA and $LiPF_6$; and (e) DBA and $LiPF_6$.

When $LiPF_6$ is added in BA or DBA, it disappears. There are two possible

mechanisms: 1) dissolution of $LiPF_6$ in amines and 2) chemical reactions of amines and $LiPF_6$. The FTIR spectra of electrolyte and EC-EMC are compared in **Figure 4.6c** and the two bands that appear in electrolyte while not in EC-EMC are attributed to the P-F vibrations in PF_6^-. [98] The band at 840 cm^{-1} and 558 cm^{-1} correspond to the P-F stretching mode and bending mode, respectively. [99] The FTIR measurements of BA-$LiPF_6$ and DBA-$LiPF_6$ mixtures are carried out after the undissolved $LiPF_6$ is removed, as shown in **Figure 4.6d** and **Figure 4.6e**. The two bands at 850 cm^{-1} and 558 cm^{-1} match the same vibrations as the PF_6^- anion in the electrolyte, suggesting that $LiPF_6$ is dissolved in BA or DBA. If $LiPF_6$ reacted with BA or DBA, the octahedral symmetry of the PF_6^- anion must have been destroyed and the P-F stretching and bending modes should have changed.

As shown in **Figure 4.4a**, adding BA or DBA in electrolyte leads to a reduction in ionic conductivity, which may be due to their dissolution of $LiPF_6$, according to the previous discussion. The donor number (DN) and the dielectric constant (ε) of the solvents play important roles in the solvation process. [100] **Table 4.2** displays the DN and ε values of BA, DBA, EC and EMC. [101-103] BA and DBA are strong Lewis bases and have larger DN than EC. The carbonyl oxygens of EC are the binding sites for Li^+ and their lone-pair electrons could effectively neutralize the coulombic attraction of Li^+. [104] The solvation shell of Li^+ would be broken apart when a cosolvent of higher DN is present. [105] BA and DBA would compete with EC on the solvation of Li^+; however, they have much smaller dielectric constants than EC and EC-EMC mixture, which means they are poor

dissociating solvents. The dissociation of Li^+ and PF_6^- ion pairs increases the population of free Li^+ cations, which helps increase the electrolyte conductivity. [89] That is, poor dissociating solvents such as BA and DBA may perturb the original Li^+ solvation shells and decrease the overall electrolyte conductivity.

Table 4.2 Donor number and dielectric constant values at 25 ℃

	BA	DBA	EC	EMC	EC:EMC (1:1)
Donor number (kcal/mol)	40	50	16.4	17.2	—
Dielectric constant	4.6	3.6	95.3	3.5	33.6

It is noticed that the addition of DBA leads to a larger reduction in electrolyte conductivity than addition of the same amount of BA (**Figure 4.4a**), which correlates well with the fact that the DBA-EC reaction is less intense than the BA-EC reaction. The consumption of EC by BA or DBA may not be the main reason for the reduction in electrolyte conductivity, since EC/EMC based electrolyte solvent has existing EC-EMC mass ratio of 3:7. Due to the intense reaction between BA and EC, BA is considerably consumed and the remaining BA for solvation perturbation is reduced, so that the extent of reduction in electrolyte conductivity is lowered.

As different amines are dropped on the cathodes and anodes harvested from fully charged (4.3 V) LIR-2450 cells, local temperatures are monitored continuously and the results are displayed in **Figure 4.7a**. For charged anodes, upon exposure to BA, there is a

slight temperature increase, which may be due to the reactions between BA and SEI. There is no temperature change when the charged anodes are exposed to DBA or THA. For charged cathodes, abrupt temperature increase is observed upon exposure to BA, DBA or THA. Charged cathode disks are then soaked up in different amines. After the cathodes are fully rinsed to remove any remaining amines, they are reassembled with fresh pristine electrolyte. The discharge capacities of the reference, BA, DBA or THA modified cells are 164 mAh g-1, 27.2 mAh g^{-1}, 149.2 mAh g^{-1} and 157.1 mAh g^{-1}, respectively (**Figure 4.7b**). The initial voltage drop of the reference cell results from the voltage relaxation. Amine-treated cathodes have larger voltage drops than the reference cathode, probably because of the redox reactions between amines and charged cathode. The charged cathode could oxidize the primary amine into oxime [106], benzylidenebenzylamine [107] or dibenzyldiazene [108], as shown in **Figure 4.7c**. Benzaldehyde oxime is solid at room temperature, which could be formed on the surface of charged cathode. The latter two are liquid and their molecular weight is confirmed by mass spectra. Secondary and tertiary amines could be oxidized into imine or amine oxides [109], and the reaction products are solid, which could also form on the surface of the charged cathode (**Figure 4.7d** and **Figure 4.7e**). No liquid reaction products are detected in the mass spectra of DBA and THA. For DBA and THA, the solid products on the surface could prevent further reactions between the charged cathodes and amines, so that the discharge capacities of DBA and THA treated cathodes are comparable with that of the reference cell. In general, capacity

losses and voltage drops of amine treated cathodes are due to the combination of cathode degradation and formation of resistive layers on electrode surfaces.

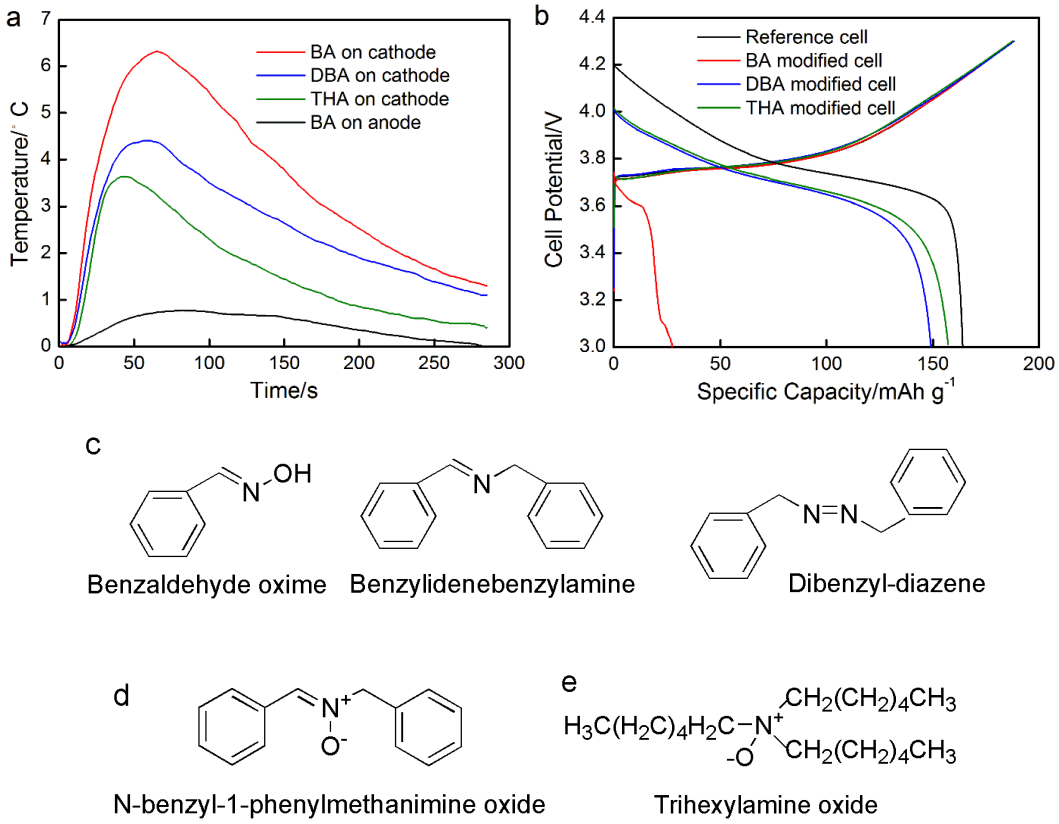

Figure 4.7 (a) Temperature changes of cathodes and anodes exposed to amines. (b) Charge-discharge plots of the reference and amine-modified cells. Reaction products between charged cathode and (c) BA, (d) DBA, and (e) THA.

To confirm the existence of resistive organic layers, XPS spectra are obtained on the surface of the amine-treated cathodes, as shown in **Figure 4.8**. N 1s peak at 399.7 eV is observed on reference cathode not treated by amines, which must be the residue from the electrolyte precipitating on cathode surface since there is no nitrogen element in cathodes. For BA treated cathode, the new component at 401.4 eV is attributed to C=N in benzaldehyde oxime. [110] There is a small amount of solid reaction product between BA

and charged cathodes and most of the reaction products are liquid, which explains the large decrease in discharge capacity of BA treated cathode, because the reactions could happen continuously without any barrier layers. The peaks at 400.9 eV for DBA treated cathode and 401.9 eV for THA treated cathode are attributed to $C=N^+$ in imine oxide and $C-N^+$ in amine oxide, respectively. [111-112] In the C 1s spectra (Figure 3.8b), the peaks assigned at 286.1 eV (C-H) and 290.7 eV (C-F) are related to the PVDF binder. [113] The peak corresponding to carbon black is observed at 284.6 eV (C-C). The peaks at 287.2 eV and 289.1 eV are assigned to C-O in carbonate salts and C=O in lithium alkyl carbonates, respectively. [114] For amines treated cathode, new C 1s peaks appear at 285.5 eV, 285.7 eV and 285.8 eV, which is attributed to C=N, $C=N^+$ and $C-N^+$ bonds in oxime, imide oxide and amine oxide, respectively. [115] It is noticed that the C-H and C-F bonds in PVDF shift to higher binding energies for all amine treated cathode. This is due to the reaction of amines with PVDF binders, since PVDF is sensitive to bases that can degrade it by creating insaturations. [116] The binding energy of C-C also shifts in amine treated cathodes. In the O 1s spectra (**Figure 4.8c**), besides the peaks for C-O (533.0 eV) and C=O (531.1 eV), the peak at 529.4 eV is assigned to the bonds between transition metals and oxygen. [117-118] Amine treated cathodes have extra peaks at 530.5 eV (N-O), 531.7 eV (N^+-O^-) and 531.0 eV (N^+-O^-), which is consistent with the N 1s and C 1s spectra. The difference of the two N^+-O^- peaks at 531.7 eV and 531.0 eV might be due to the different chemical environment of nitrogen (**Figure 4.7d** and **Figure 4.7e**). The XPS patterns of amine

treated cathode proves that organic resistive layers form on cathode surfaces, which might also correlate with the increased R_{ct} in the EIS measurements (**Figure 4.4b**).

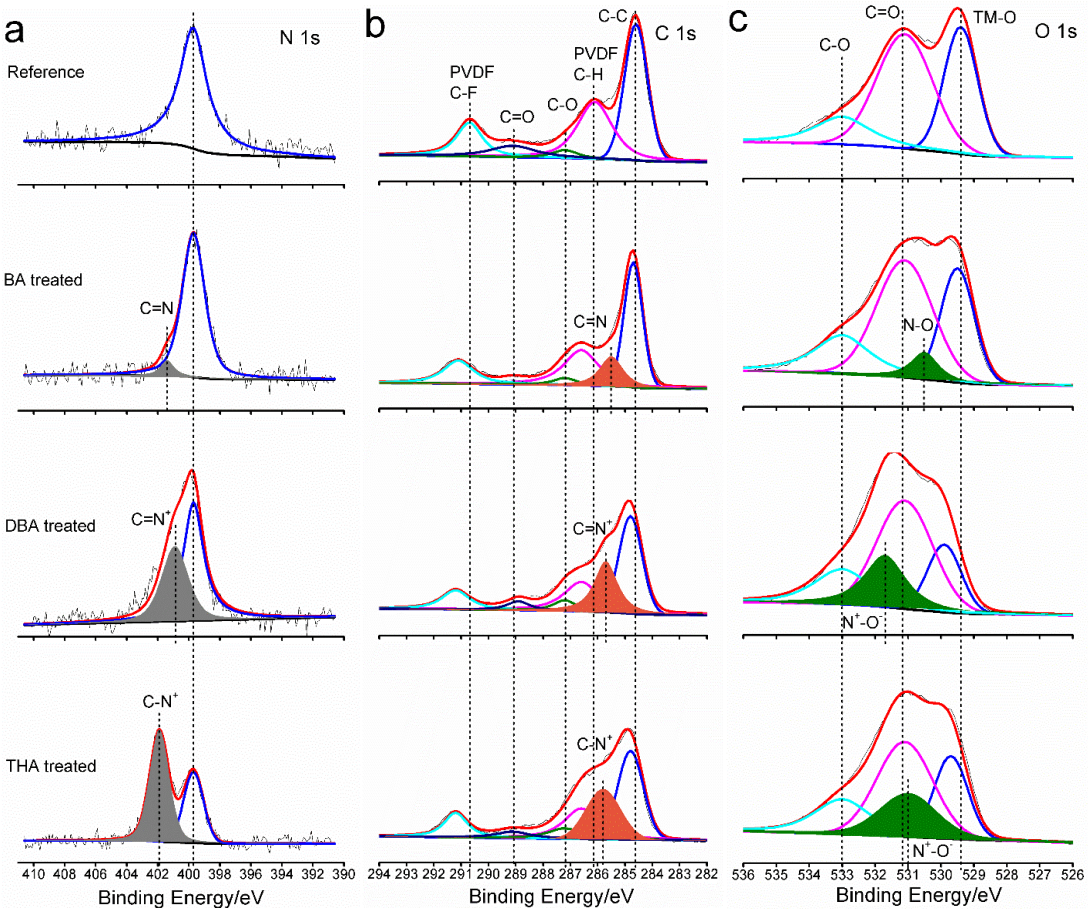

Figure 4.8 XPS patterns of reference and amine-treated cathodes: (a) N 1s (b) C 1s (c) O 1s

Coin cells based on DBA or THA treated cathodes have 91% and 96% of the capacity of reference cathode, and it is clear that the reactions between amines and cathode are exothermic (**Figure 4.7a**) is against the observed reduction in ΔT_{max}. Therefore, the cathode-DBA and cathode-THA reactions should not play a significant role in the

generation of heat during nail penetration. The perturbation of the Li^+ solvation shell by DBA and the physical barrier layer formed by THA on separator are the main factors in heat generation reduction. For BA, it is clear that there is an intense reaction between BA and charged cathodes. On the one hand, the reaction generates heat, while on the other hand, it decreases cathode voltage. The combination of the perturbation of Li^+ solvation shell by BA and the interactions of BA with charged cathode leads to the slight reduction in ΔT_{max}.

The heat generation of LIB cell may be described by an exponential function. When the temperature is below 110 °C, the heat is generated mainly from the galvanic reactions and the mild temperature increase could be balanced by heat dissipation. However, when the temperature is higher than 110 °C, exothermic chemical reactions between electrodes and electrolyte accelerate. Compared to thermally triggered TRM mechanisms which begins to function only after the heating rate starts to drastically increase, a mechanically triggered TRM method takes effect at room temperature. By suppressing the Li+ transport after TRR is released, the galvanic reactions is inhibited. If temperature can be kept below 110 °C, no aggressive exothermic reactions could take place.

This mechanically triggered method can be potentially applied to large-sized pouch cells, by embedding TRR packages in electrodes or attaching them on the inner surface of pouch cell cases. The design of geometry, material, size, and spacing of TRR

packages is crucial to the cost efficiency and scalability, which will be a crucial topic of our future research.

4.4. Conclusions

To summarize, three different amines, BA, DBA and THA, are investigated as thermal-runaway retardants (TRR) for lithium-ion batteries (LIBs). They respectively represent primary, secondary, and tertiary amines. The efficiency of thermal-runaway mitigation of THA is the highest, and that of BA is the lowest. In nail penetration test, 4 wt% THA decreases the maximum temperature rising of charged LIR 2450 cells by ~50%. The working mechanisms of the three amines are distinct. THA has a high wettability to the separator and can displace electrolyte, and therefore forms a barrier layer that blocks lithium ion transport. Both BA and DBA decrease the electrolyte ionic conductivity and elevate the charge transfer resistance. The exothermic reactions between charged cathodes and DBA or THA are not dominant factors of the decreased heat generation in nail penetration test. The exothermic reactions between charged cathode and BA is intense, and contributes to the overall heat generation of LIBs.

4.5 Acknowledgements

Chapter 4, in full, is a reprint of the material “Roles of amines for thermal-runaway-mitigating lithium-ion battery” as it appears in ACS Applied Materials and

Interfaces, Yang Shi, Daniel J. Noelle, Meng Wang, Anh V. Le, Hyojung Yoon, Minghao Zhang, Ying Shirley Meng, Yu Qiao, 2016, 8, 30956-30963. The dissertation author was the first author of this paper and conducted all the essential research work.

Chapter 5. Mitigating Thermal Runaway of Lithium-Ion Battery through Electrolyte Displacement

Alkanes are investigated as thermal-runaway retardants (TRR) for Lithium-ion battery (LIB). TRR are chemicals that can rapidly terminate exothermic reactions in LIB. Under normal working conditions they are sealed in separate packages in LIB cells, and upon mechanical abuse are released to suppress heat generation. The alkanes under investigation include octane, pentadecane, and icosane, among which pentadecane has the highest thermal-runaway mitigation (TRM) efficiency. In nail penetration test ~4 wt% pentadecane reduced the maximum temperature of fully charged LIR-2450 cell by ~60%; in impact test ~5 wt% pentadecane reduced the maximum temperature of fully charged pouch cell by ~90%. The high TRM efficiency of pentadecane is attributed to its superior wettability to the separator and its immiscibility with electrolyte. By forming a physical barrier between cathode and anode, pentadecane interrupts lithium ion (Li^+) transport and increases the charge transfer resistance by nearly two orders of magnitude. The diffusion rate of pentadecane in electrode layer stack was measured to be ~580 μm/s.

5.1. Introduction

Tremendous progress was achieved in the past a few decades in the development of Lithium-ion battery (LIB). In term of specific cost, specific energy, and energy density, LIB by far outperforms lead acid batteries, nickel metal hydride batteries, and

supercapacitors, and have been widely employed in commercial and military fields [90]. Recently, intensive research is being conducted to extend the application of LIB to large-scale energy storage systems, such as electric vehicles with driving range more than 300-400 miles [91] and smart grids on the scale of 0.6-4.3 MW [119]. As the battery structure is scaled up, the system damage tolerance becomes a bottleneck.

Under normal working condition, the cathode and the anode in a LIB are separated by a thin porous membrane, which can be ruptured if the battery is mechanically abused. Under this condition, the cathode and the anode are in direct contact, creating internal shorting sites (ISS) surrounding the damaged areas. The large amount of stored energy is rapidly dissipated in the ISS, resulting in a fast temperature increase. When the temperature rises to above 90 ˚C, a series of exothermic electrochemical reactions and chemical decompositions take place, and thermal runaway occurs [54]. Battery fire hazard imposes a tough challenge to the safety and robustness of LIB-based energy storage devices.

A promising approach to mitigate thermal runaway of LIB is to shut down the reactions when the LIB cell malfunctions. For the most adverse conditions, the shutdown mechanism must be spontaneous, independent of external control modules or integrated electronic elements. Positive-temperature-coefficient (PTC) materials may be coated on current collectors, which increases the internal impedance at 90-130 ˚C [49, 58-60]. Microspheres with low melting points are incorporated with anodes and separators, which

could cover anode surfaces when they melt, preventing further ion disintercalation [47]. However, thermal runaway has already begun at such temperatures. The shutdown process of the PTC additives and microspheres has to compete against the fast and intense local heat generation.

It is desirable that thermal-runaway mitigation (TRM) mechanism can be activated immediately after the battery is damaged, even before the temperature begins to increase. Recently we investigated mechanically triggered TRM approaches[76, 92, 120-121]. When the cell was mechanically abused, thermal-runaway retardant (TRR) was released into the battery cell to significantly reduce the heat generation rate. The amount of TRR was less than 5% so that the reduction in effective specific energy was trivial.

In our previous work, we investigated aliphatic amines as TRR[93, 122]. One promising TRM mechanism is electrolyte displacement: If the TRR is more wettable to electrodes or separator than the electrolyte, it may form a thin layer that blocks lithium ion (Li^+) transport. In the current study, a class of low-toxic chemicals, alkanes, are examined as TRR candidates. We focus on octane, pentadecane, and icosane, representing alkanes of low, intermediate, and high molecular weights, respectively.

5.2. Experimental

Nail penetration tests were performed as described in our previous work [93]. Fully charged (4.3 V) LIR-2450 cells were disassembled and re-assembled in modified cell

cases with two holes, which allowed for the injection of TRR. Immediately prior to the nail penetration, 100 μL octane, pentadecane, or pristine electrolyte (1M $LiPF_6$ in EC:EMC wt 1:1) were injected into the modified cell. Icosane was a solid alkane at room temperature. To test its influence on heat generation of damaged LIB cells, 0.1g icosane was grounded into powders and placed next to the electrodes inside re-assembled cell before nail penetration. The temperature of the cells was recorded by a thermal couple attached to the cell case.

Wettability tests and contact angle measurements (KSV Instruments CAM 100) were carried out by dropping 50 μL electrolyte or pentadecane on Celgard 2320 separators.

To evaluate the influence of pentadecane on cell resistance, coin cells were assembled with cathode films composed of $LiNi_{0.5}Co_{0.2}Mn_{0.3}O_2$, polyvinylidene fluoride, and carbon black, with the mass ratio of 93:4:3; lithium metal served as the anode. Extra pentadecane was added into the cell; the mass of pentadecane was 4% of the total mass of electrodes, separator, and electrolyte. Reference coin cell was assembled without pentadecane. Electrochemical impedance spectroscopy (EIS) measurements were carried out on the reference cell and the pentadecane-modified cell, in the frequency range of 10^6 Hz to 10^{-2} Hz with the signal amplitude of 10 mV.

Diffusion rate measurement was performed. Double-side coated cathode (MTI, bc-af-241NCM-523) and anode (MTI, bc-cf-241-ds) sheets as well as separators (Celgard

2320) were punched into disks with diameters of 63.5 mm. Three layers of cathode, three layers of anode, and six layers of separators were stacked together to form an electrode layer stack. A 3-mm-diameter hole was punched through the center of the stack. A mode made of poly(methyl methacrylate) with built-in channels for pentadecane insertion was placed on top of the electrode stack, and they were sandwiched between the compression plates of a type-5582 Instron machine, with the compression pressure of 1 kPa. 200 μL pentadecane was inserted through the built-in channel, and the diffusion distances were measured after 15 sec, 30 sec, and 45 sec.

Pouch cells embedded with TRR packages were assembled to evaluate the efficiency of TRR in large-sized LIB. Polyethylene/aluminum/polyester (PAP) trilayer (ULINE S-16893) material was folded and heat sealed to form cylindrical packages using an impulse sealer (Mcmaster-Carr). A gelatin straw was inserted into the PAP cylinder as the scaffold, and pentadecane was injected. Two batches of pouch cells were assembled with different arrangement of TRR packages. For the first batch, the cylindrical package had the diameter of ~6 mm and the length of ~35 mm. Four packages were embedded in one pouch cell and their mass percentage was 5% of the pouch cell. For the second batch, the cylindrical package had the diameter of ~6 mm and the length of ~10 mm. Five packages were embedded in one pouch cell, and their mass percentage was 2% of the pouch cell. Double-side coated cathode (MTI, bc-af-241NCM-523) and anode (MTI, bc-cf-241-ds) were cut into rectangular sheets with the length of ~60 mm and the width of

~47 mm. The electrode sheets were modified by creating four and five openings for the first and second batch, respectively. Pouch cells were assembled with 11 layers and 12 layers of modified cathode and anode sheets, respectively, embedded with empty or TRR packages. UL 1642 standard impact test was performed on the pouch cells. A stainless steel rod with the diameter of 16 mm and the length of 66.5 mm was affixed at the surface of the pouch cell. A 9-kg hammer was dropped from a distance of 0.6 m. The temperature of the cell was recorded by a thermocouple affixed at the surface.

5.3. Results and Discussion

In the nail penetration test, TRR is injected into the testing cell immediately before the nail penetration takes place [93]. Three straight-chain alkanes, namely octane, pentadecane, and icosane are tested. **Figure 5.1a** shows the temperature profiles of the cells after nail penetration. All alkanes have shown reduced peak temperature increase (ΔT_{max}) while the addition of pentadecane results in the smallest ΔT_{max}. Addition of pentadecane reduces ΔT_{max} by ~60%, from ~75 °C in reference cells to ~30 °C. **Figure 5.1b** shows the calculated heat generation in the first 20 minutes after nail penetration, using a model developed in our previous work [93]. Addition of 4 wt% pentadecane leads to ~50% reduction in heat generation, from ~0.23 Wh in reference cells to ~0.12 Wh. Octane has a lower efficiency, possibly due to its low boiling point of 125 °C. After nail penetration, the temperature inside the cells increases rapidly and causes evaporation of

octane. Icosane has a melting point of 36 °C and would be melted inside the cell after nail penetration. It could flow and wet the separator after melting, but with a higher viscosity and a shorter diffusion distance. That is, the optimum alkane TRR should have an intermediate chain length, such as pentadecane.

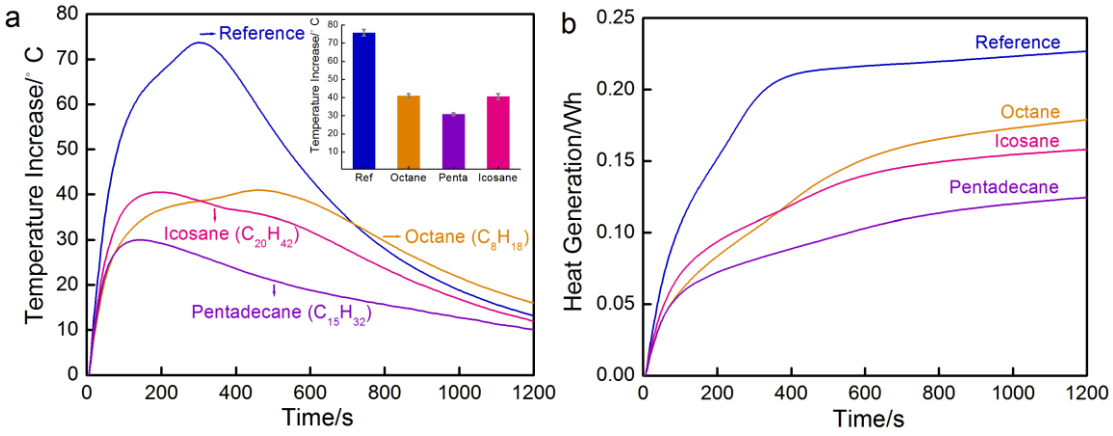

Figure 5.1 (a) Typical temperature profiles measured in nail penetration tests on reference and alkanes-modified coin cells; the inset shows the peak temperatures with error bars. (b) Calculated heat generation of reference and alkanes-modified cells.

To investigate the TRM mechanism of pentadecane, wettability and contact angle tests are performed, as shown in **Figure 5.2a**. It is evident that pentadecane could spread over a much larger area on the separator than electrolyte. The contact angle measurement further proves that pentadecane is much more wettable to the separator. Since pentadecane is not miscible with the electrolyte and is more wettable to the separator, it will repel electrolyte and form a physical blocking layer on the separator, which suppresses Li^+ transport. The EIS measurement results (**Figure 5.2b**) show that the charge transfer resistance increases by 50 times with the added pentadecane. **Figure 5.2c** illustrates the

working mechanism of pentadecane. The charge transfer reactions at the electrode-electrolyte interface are suppressed due to the accumulation of reaction products (Li^+).

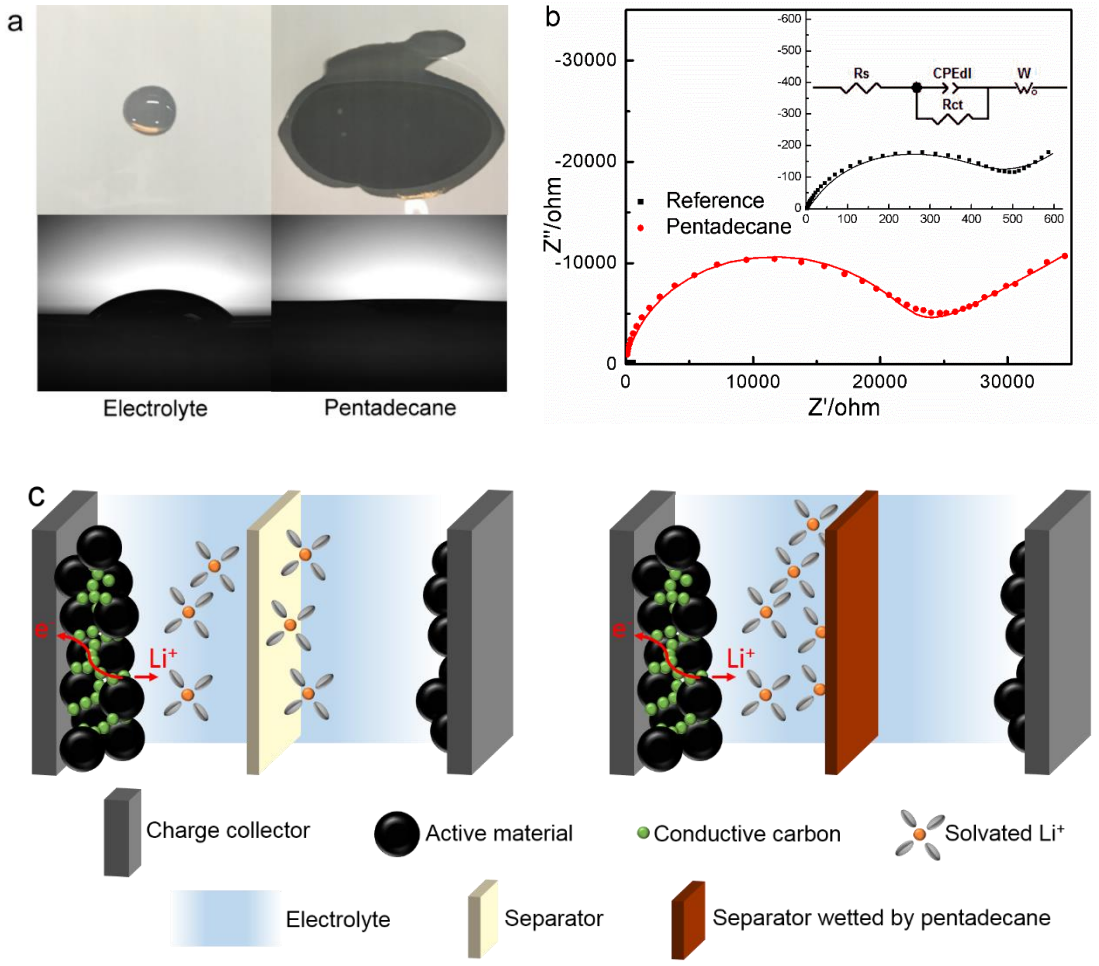

Figure 5.2 (a) Diffusion tests (above) and contact angle measurement (below) of electrolyte and pentadecane; the photos were taken after the liquid was dropped on the substrate for 15 s. (b) Nyquist plots, equivalent circuits, and fitting plots of reference and pentadecane modified coin cells. (c) Illustration of the working mechanism of pentadecane.

The diffusion rate of pentadecane in electrode layers is a key parameter for TRM [55]. The diffusion rate measurement setup is illustrated in **Figure 5.3a**. Longitudinal

wicking from an reservoir occurs when the liquid wets the porous layered structure [123]. The diffusion distance, l, of a liquid flowing under capillary pressure is given by the Washburn-Lucas equation [124].

$$l^2 = \left(\frac{\gamma}{\eta} \frac{\cos\theta}{2} \right) rt$$

where γ is the liquid surface tension, η is the liquid viscosity, θ is the contact angle, r is the effective capillary radius, and t is time. It shows a linear relationship between t and l^2, fitting well with **Figure 5.3b**. The surface tension and viscosity of pentadecane are 25.8 mN/m and 2.841 cP, respectively [125]. The contact angle of pentadecane on separators and electrodes are 0°. **Figure 5.3c** shows typical figures of cathode, anode, and separator after diffusion tests. The wetted areas show circular or elliptical shapes. The diffusion distance is defined as the radius of circle or the average of semi-major and semi-minor axes of ellipse. The calculated effective capillary radius are 33.1 μm, 31.6 μm, and 22.7 μm for anode, cathode, and separator, respectively. When the electrode stack is compressed at a pressure of 1 kPa, pentadecane could travel 8.7 mm on separator in 15 seconds. Such a measurement is conservative, since in a LIB cell nail penetration or impact would damage local electrodes, leading to a loosely packed electrode structure that favors the capillary flow of pentadecane.

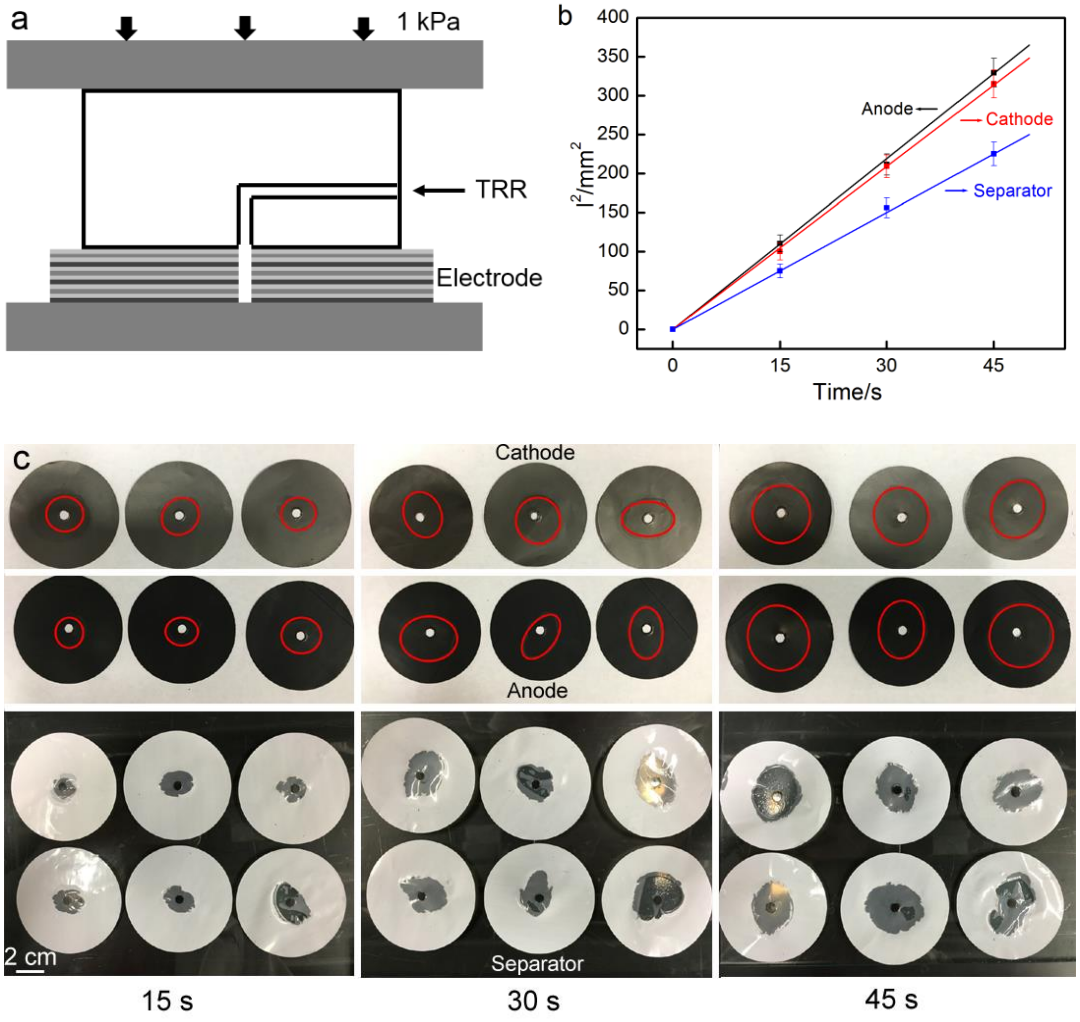

Figure 5.3 (a) Schematic of the diffusion rate measurement setup. (b) The relationship between the diffusion distance (l) and time (t). (c) Typical photos of cathode, anode and separator in the diffusion rate measurement experiment.

In order to incorporate TRR into a large-sized pouch cell, the electrodes are modified to host TRR packages. The parameters of pouch cells under investigation are shown in **Table 5.1**. Impact tests were performed on two batches of pouch cells (B1 and B2) with different percentage of TRR. The designed modified electrodes are illustrated in

Figure 5.4 a-b and their temperature profiles are shown in **Figure 5.4 c-d**. The maximum temperature increase (ΔT_{max}) of pouch cell embedded with 5% TRR is only 5 °C, order-of-magnitude lower than that of reference cell (**Figure 5.4c**). With a decreased TRR percentage, ΔT_{max} is reduced by ~50% (**Figure 5.4d**). **Figure 5.4 e-f** display the disassembled B2 pouch cells embedded with empty packages and TRR packages; all the packages are broken apart and TRR are released after impact.

Table 5.1 Parameters of LIB pouch cells

	Capacity	Voltage	Mass	Impedance
Batch 1-Reference cell	0.754 Ah	4.20 V	20.0 g	19.58 mΩ
Batch 1-5% TRR cell	0.706 Ah	4.20 V	21.0 g	19.78 mΩ
Batch 2-Reference cell	1.0785 Ah	4.20 V	28.2 g	15.90 mΩ
Batch 2-2% TRR cell	1.0820 Ah	4.20 V	28.8 g	15.12 mΩ

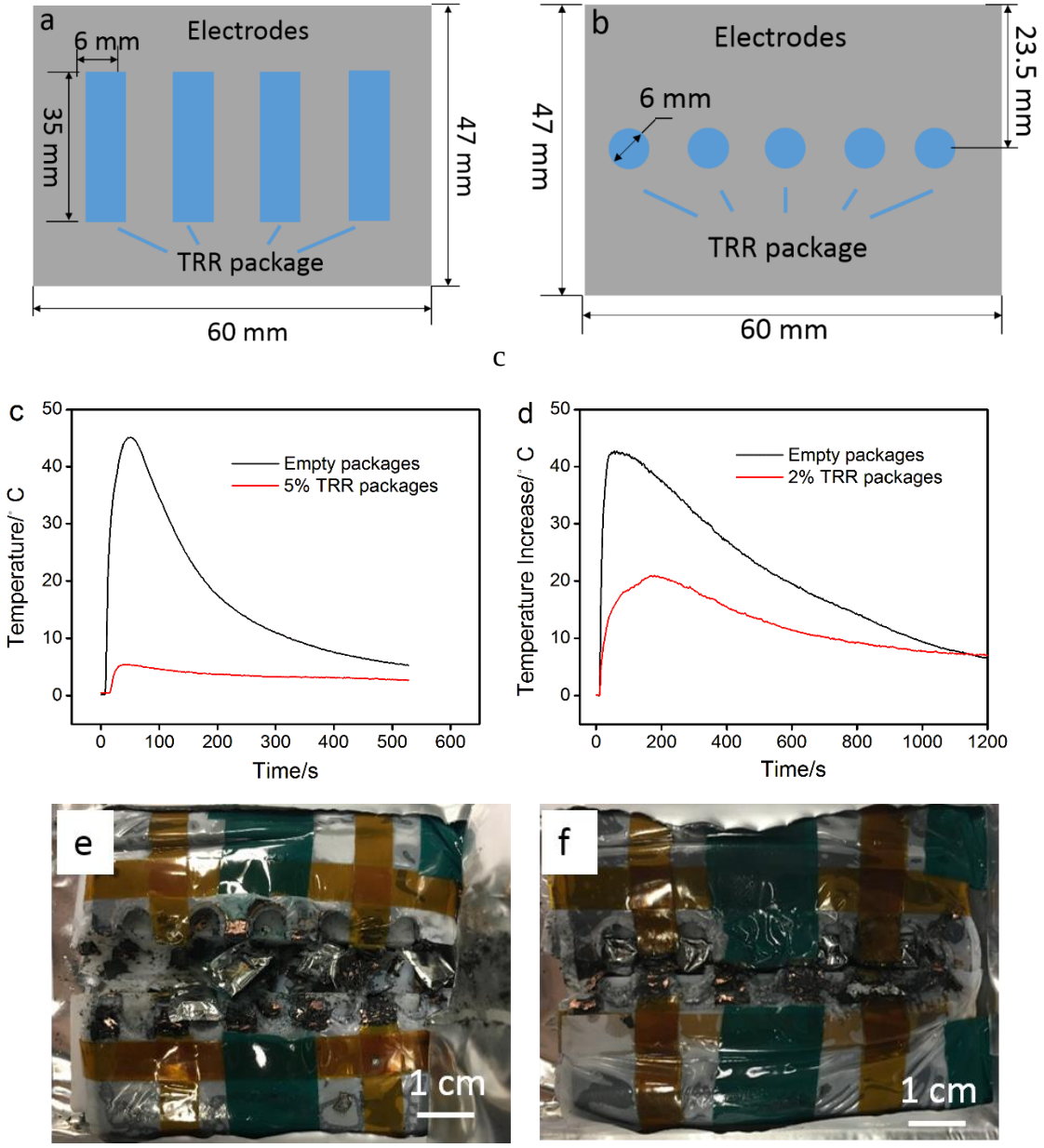

Figure 5.4 Modified electrode designs of (a) B1 pouch cells and (b) B2 pouch cells; temperature profiles of (c) B1 pouch cells and (b) B2 pouch cells; disassembled B2 pouch cells with (e) empty and (f) TRR packages.

5.4. Conclusion

Pentadecane is identified as an efficient and low-toxic thermal-runaway retardant (TRR) of lithium-ion battery (LIB). In nail penetration test of coin cells, 4 wt% pentadecane reduces the peak temperature by ~60%, better than octane and icosane; in impact test of pouch cells, 5 wt% pentadecane reduces the peak temperature by nearly an order of magnitude and 2 wt% pentadecane reduces the peak temperature by ~50%. The working mechanism of pentadecane is associated with its superior wettability to the separator material. Through electrolyte displacement, Li^+ transport is suppressed; with 4 wt% pentadecane, charge transfer resistance of electrolyte is increased by 50 times. Diffusion rate measurement demonstrates that pentadecane can travel 8.7 mm in 15 seconds in an electrode layer stack.

5.5 Acknowledgements

Chapter 5, in part, is currently being submitted for publication of the material "Mitigating thermal runaway of lithium-ion battery through electrolyte displacement", Yang Shi, Daniel J. Noelle, Meng Wang, Anh V. Le, Hyojung Yoon, Minghao Zhang, Ying Shirley Meng, Jiang Fan, Dengguo Wu, Yu Qiao, 2016. The dissertation author was the first author of this paper and conducted all the essential research work.

Chapter 6. High Energy Density Cells

6.1. Introduction

Li-rich layered oxides (LRLO) are promising candidates for cathode materials, thanks to their high operation voltage and high specific capacity [126]. Currently, the large first cycle irreversibility and the inferior rate capability limit its application, and intensive study is being carried out to enhance its electrochemical performance. Since LRLO has much higher energy density than today's active materials, it may potentially impose more critical challenges to battery system safety [127]. It is imperative to investigate the effect of TRR on mechanically abused LRLO cells, so as to evaluate the adaptiveness of our thermal-runaway mitigation technology to near-future battery chemistry.

6.2. Experimental

Two kinds of LRLO material (LRLO-1 and LRLO-2) were used as the active material. Their compositions are Li ($Li_{0.167}Mn_{0.5}Ni_{0.167}Co_{0.167}$) O_2 and Li ($Li_{0.144}Mn_{0.544}Ni_{0.136}Co_{0.136}$) O_2, respectively. The composite electrodes are composed of powders, polyvinylidene fluoride (PVDF, Kynar 710), and carbon black (Timcal, Super C65), in weight ratio of 80:10:10. The active material was provided by Professor Shirley Meng's group at the Department of Nanoengineering, University of California - San Diego. 2g of the three components were mixed in 1.8 mL 1-Methyl-2-pyrrolidinone (NMP, anhydrous, 99.5%, Sigma Aldrich. The mixing was performed in a 5 mL beaker by a

ultrasonic processor (Qsonica Q55) for 20 min. The slurry was casted on an aluminum foil using a doctor blade, and dried in vacuum at 80 °C for 24 h. The active mass loading of the cathode was 8.7 mg/cm^2.

Disc electrodes were punched out by using a hammer driven punch with an diameter of 14.3 mm, compressed by passing through a steel rolling mill, and dried in vacuum oven at 80 ^{o}C for 12 h, before placing them into an Ar-filled glovebox (H_2O < 0.1 ppm). Type-2016 coin cells were assembled with Li metal discs (1.1 mm in diameter) as anodes, 1 M $LiPF_6$ in ethylene carbonate and diethyl methyl carbonate (EC: EMC 1:1 wt) as electrolyte, and trilayer PP/PE/PP films (2320, Celgard Inc) as separators.

The coin cells were allowed to rest for 2 h before being charged to 4.8 V at C/10 (1C = 250 mA g^{-1}). The charged cells were disassembled and reassembled with modified cell cases in the glovebox. The modified cases had 2 holes near the sealing O-ring, with the diameter of 1 mm. The holes were covered by Kapton tapes before nail test. Pentadecane was injected through the holes via a syringe. Immediately after the injection, a stainless steel nail with the diameter of 1.6 mm was penetrated through the cell by a vise, and the temperature was recorded by a Type-K thermocouple at the same time. The mass of pentadecane ranges from 2% to 5% of the mass of coin cells including cell case.

6.3. Results and Discussion

The charge curve of LRLO is displayed in **Figure 6.1**. The voltage plateau is at

~4.6 V vs. Li^+/Li^0. The nail test setup is shown in **Figure 6.2**. Before nail test, the voltage of all the cells are ~4.65 V. For LRLO-1, as shown in **Figure 6.3a**, by adding 3.5 wt% pentadecane, the maximum temperature increase is reduced by ~50%. For LRLO-2, it shows a similar peak temperature reduction, as displayed in **Figure 6.3b**. These results suggest that pentadecane can work efficiently for high-energy-density cathode materials.

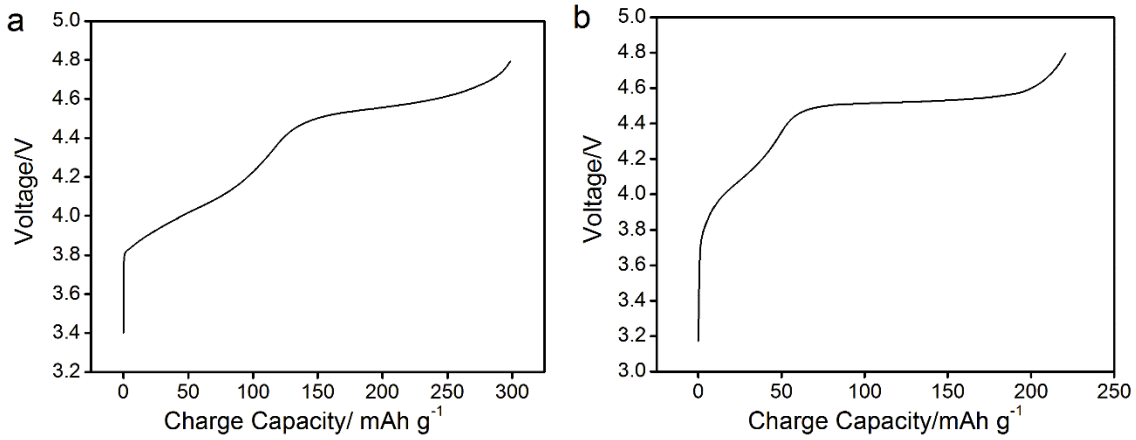

Figure 6.1 Voltage profile of the 1st charging of (a) LRLO-1 cell and (b) LRLO-2 cell

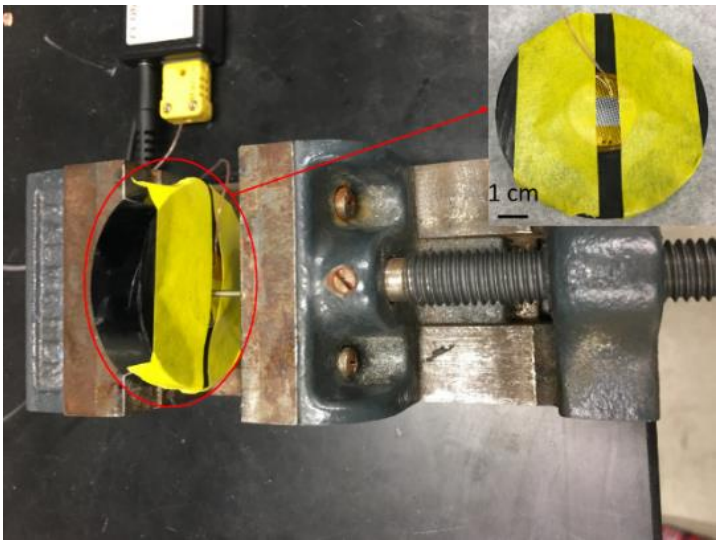

Figure 6.2 Nail test setup; the inset shows a modified cell

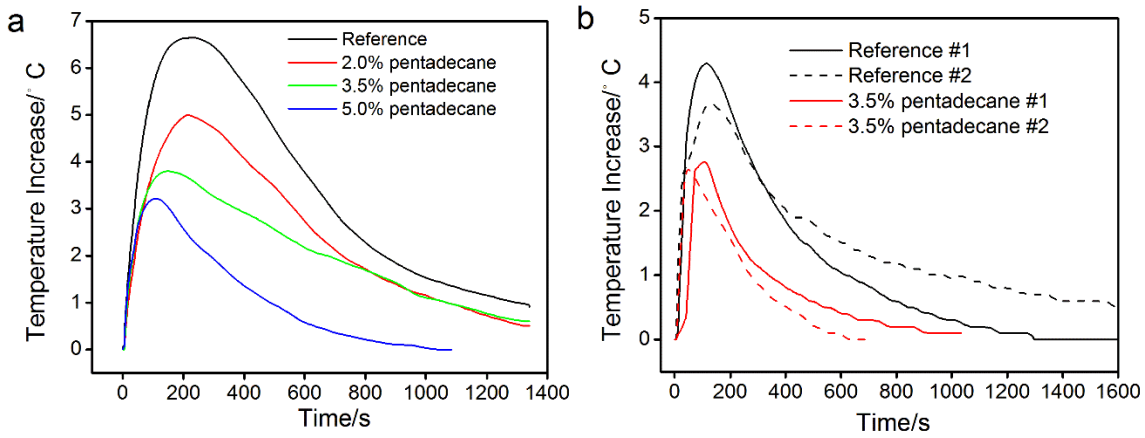

Figure 6.3 Nail test temperature profiles of (a) LRLO-1 and (b) LRLO-2 cells

Chapter 7. Summary and Future Work

The central thrust of the current study is to identify aggressive thermal-runaway retardant (TRR) candidates. Due to the high energy density in lithium-ion battery (LIB), the working mechanism of TRR should be physical, preferably through suppression of lithium ion (Li^+) transport. Promising approaches include decreasing electrolyte conductivity and creating barrier layers. Reduction in electrolyte conductivity could be achieved by interrupting the Li^+ solvation shell; barrier layers could be at either the separator or the electrode surfaces.

We investigated a large number of TRR candidates and two classes of chemicals are chosen: amines and alkanes. Secondary and tertiary amines could efficiently decrease the maximum temperature increase in nail penetration and impact tests, and tertiary amines perform slightly better. Primary amines does not efficiently decrease the temperature increase. For secondary amines, the working mechanism is mainly associated with the reduction of electrolyte conductivity. For tertiary amines, the working mechanism is mainly related to its immiscibility with electrolyte and the high wettability on separator. The working mechanism of alkanes is similar to that of tertiary amine. Alkanes have superior wettability on separators, and they do not react with the electrodes. Since the reactions with electrodes are exothermic and alkanes have low toxicity, they are the most promising TRR among all the candidates under investigation. Alkanes with different chain lengths have different performance. Alkanes with longer chains have

higher viscosity, which has detrimental effects on diffusion rate; shorter-chained alkanes have low boiling points, which leads to quick evaporation. Among various alkanes, pentadecane is the most efficient TRR. About 5 wt% pentadecane reduced the maximum temperature increase of fully charged pouch cell by ~90%. In high energy density coin cells with Li-rich layered oxide cathodes, pentadecane could also work well.

Our experiments suggest that the following thermal-runaway mitigation methods are relatively inefficient: fire extinguishing additives, electrolyte superabsorbent, and gas-generation additives in composite electrode. Hydrazides, for example, can generate a large amount of gas when heated; however, the large amount of heat released in the gas generation process lowers the overall efficacy.

The selection of TRR package material is based on two criteria. Firstly, it should be nonconductive and have little influence on the normal performance of LIB. Secondly, it must be highly impermeable. A trilayer material is chosen. The outer layer is made of polymer inert in the battery environment; it could be thermally sealed, which avoids the use of glues unstable in electrolyte. The inner aluminum layer serves as the diffusion barrier of the enclosed TRR. Our testing data showed that the packages did not affect the cycling performance of LIB.

Future work on thermal-runaway mitigation will be focused on package design and efficient delivery of TRR, as well as application of TRR in high-energy battery chemistry. In future design, interconnecting channels could be fabricated. Once exposed

to mechanical loading, the broken sites of TRR package could serve as outlet, allowing TRR to rush out and disperse into the electrode stacks. Using pressure sensitive materials is also a promising direction. Since LIB cells are under inner pressure during normal operation, the embedment of pressure sensitive materials should not cause unexpected battery failures associated with volume expansion and internal stresses during cycling.

References

1. Balakrishnan, P. G.; Ramesh, R.; Kumar, T. P., *Journal of Power Sources* 2006, *155,* 401-414.

2. Pinson, M. B.; Bazant, M. Z., *Journal of the Electrochemical Society* 2012, *160,* A243-A250.

3. Wang, Q. S.; Ping, P.; Zhao, X. J.; Chu, G. Q.; Sun, J. H.; Chen, C. H., *Journal of Power Sources* 2012, *208,* 210-224.

4. Yang, H.; Amiruddin, S.; Bang, H. J.; Sun, Y. K.; Prakash, J., *Journal of Industrial and Engineering Chemistry* 2006, *12,* 12-38.

5. Bandhauer, T. M.; Garimella, S.; Fuller, T. F., *Journal of the Electrochemical Society* 2011, *158,* R1-R25.

6. Wang, Q. S.; Sun, J. H.; Yao, X. L.; Chen, C. H., *Journal of the Electrochemical Society* 2006, *153,* A329-A333.

7. Wang, Q. S.; Sun, J. H.; Yao, X. L.; Chen, C. H., *Thermochimica Acta* 2005, *437,* 12-16.

8. Sloop, S. E.; Pugh, J. K.; Wang, S.; Kerr, J. B.; Kinoshita, K., *Electrochemical and Solid State Letters* 2001, *4,* A42-A44.

9. Zinigrad, E.; Larush-Asraf, L.; Gnanaraj, J. S.; Sprecher, M.; Aurbach, D., *Thermochimica Acta* 2005, *438,* 184-191.

10. Cho, J.; Kim, Y. W.; Kim, B.; Lee, J. G.; Park, B., *Angewandte Chemie-International Edition* 2003, *42,* 1618-1621.

11. Cho, J.; Kim, T. J.; Kim, J.; Noh, M.; Park, B., *Journal of the Electrochemical Society* 2004, *151,* A1899-A1904.

12. Kweon, H. J.; Park, J.; Seo, J.; Kim, G.; Jung, B.; Lim, H. S., *Journal of Power Sources* 2004, *126,* 156-162.

13. Yang, Z. X.; Yang, W. S.; Evans, D. G.; Li, G.; Zhao, Y. Y., *Electrochemistry*

Communications 2008, *10,* 1136-1139.

14. Xia, L.; Li, S. L.; Ai, X. P.; Yang, H. X.; Cao, Y. L., *Energy & Environmental Science*

4, 2845-2848.

15. Park, Y. S.; Bang, H. J.; Oh, S. M.; Sun, Y. K.; Lee, S. M., *Journal of Power Sources* 2009, *190*, 553-557.

16. Shim, E. G.; Nam, T. H.; Kim, J. G.; Kim, H. S.; Moon, S. I., *Journal of Power Sources* 2007, *172*, 919-924.

17. Nam, T. H.; Shim, E. G.; Kim, J. G.; Kim, H. S.; Moon, S. I., *Journal of the Electrochemical Society* 2007, *154*, A957-A963.

18. Xiang, H. F.; Xu, H. Y.; Wang, Z. Z.; Chen, C. H., *Journal of Power Sources* 2007, *173*, 562-564.

19. Feng, J. K.; Ai, X. P.; Cao, Y. L.; Yang, H. X., *Journal of Power Sources* 2008, *177*, 194-198.

20. Shim, E. G.; Nam, T. H.; Kim, J. G.; Kim, H. S.; Moon, S. I., *Electrochimica Acta* 2007, *53*, 650-656.

21. Dunn, R. P.; Kafle, J.; Krause, F. C.; Hwang, C.; Ratnakumar, B. V.; Smart, M. C.; Lucht, B. L., *Journal of The Electrochemical Society* 2012, *159*, A2100-A2108.

22. Ping, P.; Wang, Q. S.; Sun, J. H.; Xia, X.; Dahn, J. R., *Journal of the Electrochemical Society* 2012, *159*, A1467-A1473.

23. Xin, X.; Ping, P.; Dahn, J. R., *Journal of the Electrochemical Society* 2012, *159*, A1460-A1466.

24. Xu, K.; Zhang, S. S.; Allen, J. L.; Jow, T. R., *Journal of the Electrochemical Society* 2002, *149*, A1079-A1082.

25. Xu, K.; Ding, M. S.; Zhang, S. S.; Allen, J. L.; Jow, T. R., *Journal of the Electrochemical Society* 2003, *150*, A161-A169.

26. Doughty, D. H.; Roth, E. P.; Crafts, C. C.; Nagasubramanian, G.; Henriksen, G.; Amine, K., *Journal of Power Sources* 2005, *146*, 116-120.

27. Mandal, B. K.; Padhi, A. K.; Shi, Z.; Chakraborty, S.; Filler, R., *Journal of Power Sources* 2006, *161*, 1341-1345.

28. Fei, S. T.; Allcock, H. R., *Journal of Power Sources* 2010, *195*, 2082-2088.

29. Hu, J. L.; Jin, Z. X.; Hong, H.; Zhan, H.; Zhou, Y. H.; Li, Z. Y., *Journal of Power Sources* 2012, *197,* 297-300.

30. Hyung, Y. E.; Vissers, D. R.; Amine, K., *Journal of Power Sources* 2003, *119,* 383-387.

31. Wang, X. M.; Yasukawa, E.; Kasuya, S., *Journal of the Electrochemical Society* 2001, *148,* A1058-A1065.

32. Ota, H.; Kominato, A.; Chun, W. J.; Yasukawa, E.; Kasuya, S., *Journal of Power Sources* 2003, *119,* 393-398.

33. Shim, E. G.; Nam, T. H.; Kim, J. G.; Kim, H. S.; Moon, S. I., *Electrochimica Acta* 2009, *54,* 2276-2283.

34. Li, Y. J.; Zhan, H.; Wu, L.; Li, Z. Y.; Zhou, Y. H., *Solid State Ionics* 2006, *177,* 1179-1183.

35. Zhang, S. S.; Xu, K.; Jow, T. R., *Electrochemical and Solid State Letters* 2002, *5,* A206-A208.

36. Zhang, S. S.; Xu, K.; Jow, T. R., *Journal of Power Sources* 2003, *113,* 166-172.

37. Nam, N. D.; Park, I. J.; Kim, J. G., *Metals and Materials International* 2012, *18,* 189-196.

38. Xu, H. Y.; Xie, S.; Wang, Q. Y.; Yao, X. L.; Wang, Q. S.; Chen, C. H., *Electrochimica Acta* 2006, *52,* 636-642.

39. Tsujikawa, T.; Yabuta, K.; Matsushita, T.; Matsushima, T.; Hayashi, K.; Arakawa, M., *Journal of Power Sources* 2009, *189,* 429-434.

40. Lee, C. W.; Venkatachalapathy, R.; Prakash, J., *Electrochemical and Solid State Letters* 2000, *3,* 63-65.

41. Izquierdo-Gonzales, S.; Li, W. T.; Lucht, B. L., *Journal of Power Sources* 2004, *135,* 291-296.

42. Dalavi, S.; Xu, M. Q.; Ravdel, B.; Zhou, L.; Lucht, B. L., *Journal of the Electrochemical Society* 2010, *157,* A1113-A1120.

43. Kim, G. T.; Jeong, S. S.; Joost, M.; Rocca, E.; Winter, M.; Passerini, S.; Balducci, A., *Journal of Power Sources* 2011, *196,* 2187-2194.

44. Xia, X.; Ping, P.; Dahn, J. R., *Journal of the Electrochemical Society* 2012, *159*, A1834-A1837.

45. Wu, B. B.; Pei, F.; Wu, Y.; Mao, R. J.; Ai, X. P.; Yang, H. X.; Cao, Y. L., *Journal of Power Sources* 2013, *227*, 106-110.

46. Zhang, Z. C.; Zhang, L.; Schlueter, J. A.; Redfern, P. C.; Curtiss, L.; Amine, K., *Journal of Power Sources* 2010, *195*, 4957-4962.

47. Baginska, M.; Blaiszik, B. J.; Merriman, R. J.; Sottos, N. R.; Moore, J. S.; White, S. R., *Advanced Energy Materials* 2012, *2*, 583-590.

48. Xia, L.; Wang, D. D.; Yang, H. X.; Cao, Y. L.; Ai, X. P., *Electrochemistry Communications* 2012, *25*, 98-100.

49. Feng, X. M.; Ai, X. P.; Yang, H. X., *Electrochemistry Communications* 2004, *6*, 1021-1024.

50. Kise, M.; Yoshioka, S.; Hamano, K.; Kuriki, H.; Nishimura, T.; Urushibata, H.; Yoshiyasu, H., *Journal of the Electrochemical Society* 2005, *152*, A1516-A1520.

51. Kise, M.; Yoshioka, S.; Hamano, K.; Kuriki, H.; Nishimura, T.; Urushibata, H., *Journal of the Electrochemical Society* 2006, *153*, A1004-A1011.

52. Zhong, H.; Kong, C.; Zhan, H.; Zhan, C. M.; Zhou, Y. H., *Journal of Power Sources* 2012, *216*, 273-280.

53. Lu, L.; Han, X.; Li, J.; Hua, J.; Ouyang, M., *Journal of Power Sources* 2013, *226*, 272-288.

54. Finegan, D. P.; Scheel, M.; Robinson, J. B.; Tjaden, B.; Hunt, I.; Mason, T. J.; Millichamp, J.; Di Michiel, M.; Offer, G. J.; Hinds, G.; Brett, D. J. L.; Shearing, P. R., *Nat Commun* 2015, *6*.

55. Balakrishnan, P. G.; Ramesh, R.; Prem Kumar, T., *Journal of Power Sources* 2006, *155*, 401-414.

56. Arora, P.; Zhang, Z., *Chemical Reviews* 2004, *104*, 4419-4462.

57. Laman, F. C.; Gee, M. A.; Denovan, J., *Journal of The Electrochemical Society* 1993, *140*, L51-L53.

58. Zhong, H.; Kong, C.; Zhan, H.; Zhan, C.; Zhou, Y., *Journal of Power Sources* 2012,

216, 273-280.

59. Li, J.; Chen, J. G.; Lu, H.; Jia, M.; Jiang, L. X.; Lai, Y. Q.; Zhang, Z. A., *International Journal of Electrochemical Science* 2013, *8*, 5223-5231.

60. Zhang, H.; Pang, J.; Ai, X.; Cao, Y.; Yang, H.; Lu, S., *Electrochimica Acta* 2016, *187*, 173-178.

61. Yim, T.; Park, M.-S.; Woo, S.-G.; Kwon, H.-K.; Yoo, J.-K.; Jung, Y. S.; Kim, K. J.; Yu, J.-S.; Kim, Y.-J., *Nano Letters* 2015, *15*, 5059-5067.

62. Xia, L.; Wang, D.; Yang, H.; Cao, Y.; Ai, X., *Electrochemistry Communications* 2012, *25*, 98-100.

63. Abraham, D. P.; Roth, E. P.; Kostecki, R.; McCarthy, K.; MacLaren, S.; Doughty, D. H., *Journal of Power Sources* 2006, *161*, 648-657.

64. Hu, J.; Jin, Z.; Zhong, H.; Zhan, H.; Zhou, Y.; Li, Z., *Journal of Power Sources* 2012, *197*, 297-300.

65. Lai, Y.; Ren, C.; Lu, H.; Zhang, Z.; Li, J., *Journal of The Electrochemical Society* 2012, *159*, A1267-A1272.

66. Park, I.-J.; Nam, T.-H.; Kim, J.-G., *Journal of Power Sources* 2013, *244*, 122-128.

67. Ohmi, N.; Nakajima, T.; Ohzawa, Y.; Koh, M.; Yamauchi, A.; Kagawa, M.; Aoyama, H., *Journal of Power Sources* 2013, *221*, 6-13.

68. Wu, B.; Pei, F.; Wu, Y.; Mao, R.; Ai, X.; Yang, H.; Cao, Y., *Journal of Power Sources* 2013, *227*, 106-110.

69. Aurbach, D.; Srur-Lavi, O.; Ghanty, C.; Dixit, M.; Haik, O.; Talianker, M.; Grinblat, Y.; Leifer, N.; Lavi, R.; Major, D. T.; Goobes, G.; Zinigrad, E.; Erickson, E. M.; Kosa, M.; Markovsky, B.; Lampert, J.; Volkov, A.; Shin, J.-Y.; Garsuch, A., *Journal of The Electrochemical Society* 2015, *162*, A1014-A1027.

70. Aboulaich, A.; Ouzaouit, K.; Faqir, H.; Kaddami, A.; Benzakour, I.; Akalay, I., *Materials Research Bulletin* 2016, *73*, 362-368.

71. Bian, X.; Fu, Q.; Bie, X.; Yang, P.; Qiu, H.; Pang, Q.; Chen, G.; Du, F.; Wei, Y., *Electrochimica Acta* 2015, *174*, 875-884.

72. Wang, D.; Li, X.; Wang, Z.; Guo, H.; Chen, X.; Zheng, X.; Xu, Y.; Ru, J.,

Electrochimica Acta 2015, *174*, 1225-1233.

73. Lee, Y.-S.; Shin, W.-K.; Kannan, A. G.; Koo, S. M.; Kim, D.-W., *ACS Applied Materials & Interfaces* 2015, *7*, 13944-13951.

74. Chen, J. J.; Li, Z. D.; Xiang, H. F.; Wu, W. W.; Cheng, S.; Zhang, L. J.; Wang, Q. S.; Wu, Y. C., *RSC Advances* 2015, *5*, 3031-3038.

75. Shi, Y.; Zhang, M.; Qian, D.; Meng, Y. S., *Electrochimica Acta* 2016, *203*, 154-161.

76. Le, A. V.; Wang, M.; Shi, Y.; Noelle, D.; Qiao, Y.; Lu, W., *Journal of Applied Physics* 2015, *118*, 085312.

77. Le, A. V.; Wang, M.; Shi, Y.; Noelle, D. J.; Qiao, Y., *Journal of Physics D: Applied Physics* 2015, *48*, 385501-385507.

78. M. Wang, A. V. L., Y. Shi, D.J. Noelle, H. Yoon, M. Zhang, Y.S. Meng, Y. Qiao,, *J. Mater. Sci. Tech.* 2016.

79. C. Lan, X. J., Y. Qiao, Y. Ma, *Appl. Thermal Eng.* 2016.

80. Feng, X.; Weng, C.; Ouyang, M.; Sun, J., *Applied Energy* 2016, *161*, 168-180.

81. Zhao, R.; Liu, J.; Gu, J., *Applied Energy* 2016, *173*, 29-39.

82. Ni, J.; Zhou, H.; Chen, J.; Zhang, X., *Electrochimica Acta* 2008, *53*, 3075-3083.

83. Zhao, J.; Wang, L.; He, X.; Wan, C.; Jiang, C., *Journal of The Electrochemical Society* 2008, *155*, A292-A296.

84. Zugmann, S.; Fleischmann, M.; Amereller, M.; Gschwind, R. M.; Wiemhöfer, H. D.; Gores, H. J., *Electrochimica Acta* 2011, *56*, 3926-3933.

85. Riley, M.; Fedkiw, P. S.; Khan , S. A., *Journal of The Electrochemical Society* 2002, *149*, A667-A674.

86. Evans, J.; Vincent, C. A.; Bruce, P. G., *Polymer* 1987, *28*, 2324-2328.

87. Capiglia, C.; Saito, Y.; Kageyama, H.; Mustarelli, P.; Iwamoto, T.; Tabuchi, T.; Tukamoto, H., *Journal of Power Sources* 1999, *81–82*, 859-862.

88. Lee, H. S.; Sun, X.; Yang, X. Q.; McBreen, J., *Journal of The Electrochemical Society* 2002, *149*, A1460-A1465.

89. Sun, X.; Lee, H. S.; Yang, X. Q.; McBreen, J., *Journal of The Electrochemical Society* 1999, *146*, 3655-3659.

90. Etacheri, V.; Marom, R.; Elazari, R.; Salitra, G.; Aurbach, D., *Energy & Environmental Science* 2011, *4*, 3243-3262.

91. Thackeray, M. M.; Wolverton, C.; Isaacs, E. D., *Energy & Environmental Science* 2012, *5*, 7854-7863.

92. Wang, M.; Le, A. V.; Noelle, D. J.; Shi, Y.; Yoon, H.; Zhang, M.; Meng, Y. S.; Qiao, Y., *International Journal of Damage Mechanics* 2016.

93. Shi, Y.; Noelle, D. J.; Wang, M.; Le, A. V.; Yoon, H.; Zhang, M.; Meng, Y. S.; Qiao, Y., *Journal of Power Sources* 2016, *326*, 514-521.

94. Clements, J. H., *Industrial & Engineering Chemistry Research* 2003, *42*, 663-674.

95. Ikezawa, Y.; Nishi, H., *Electrochimica Acta* 2008, *53*, 3663-3669.

96. Mahmood, N.; Khan, A. U.; Sohail Khan, M.; Ali, Z.; Haq, A.-U.; Wutzler, A., *Journal of Applied Polymer Science* 2011, *122*, 1012-1018.

97. Gnanaraj, J. S.; Zinigrad, E.; Asraf, L.; Gottlieb, H. E.; Sprecher, M.; Schmidt, M.; Geissler, W.; Aurbach, D., *Journal of The Electrochemical Society* 2003, *150*, A1533-A1537.

98. Kock, L. D.; Lekgoathi, M. D. S.; Crouse, P. L.; Vilakazi, B. M., *Journal of Molecular Structure* 2012, *1026*, 145-149.

99. Yang, H.; Zhuang, G. V.; Ross Jr, P. N., *Journal of Power Sources* 2006, *161*, 573-579.

100. Sekhon, S. S.; Arora, N.; Singh, H. P., *Solid State Ionics* 2003, *160*, 301-307.

101. Marcus, Y., *Journal of Solution Chemistry* 1984, *13*, 599-624.

102. Hall, D. S.; Self, J.; Dahn, J. R., *The Journal of Physical Chemistry C* 2015, *119*, 22322-22330.

103. Maryott, A. A.; Smith, E. R., *Circulars of the National Bureau of Standards* 1951, 44 pp.-44 pp.

104. Takeuchi, M.; Matubayasi, N.; Kameda, Y.; Minofar, B.; Ishiguro, S.-i.; Umebayashi,

Y., *The Journal of Physical Chemistry B* 2012, *116,* 6476-6487.

105. Xu, K., *Chemical Reviews* 2014, *114,* 11503-11618.

106. Suzuki, K.; Watanabe, T.; Murahashi, S.-I., *The Journal of Organic Chemistry* 2013, *78,* 2301-2310.

107. Khusnutdinov, R. I.; Baygusina, A. R.; Aminov, R. I., *Russian Journal of Organic Chemistry* 2012, *48,* 1059-1061.

108. Biradar, A. V.; Kotbagi, T. V.; Dongare, M. K.; Umbarkar, S. B., *Tetrahedron Letters* 2008, *49,* 3616-3619.

109. Colladon, M.; Scarso, A.; Strukul, G., *Green Chemistry* 2008, *10,* 793-798.

110. Wang, F.; Li, H.; Liu, Q.; Li, Z.; Li, R.; Zhang, H.; Liu, L.; Emelchenko, G. A.; Wang, J., *Scientific Reports* 2016, *6,* 19367.

111. Choudhury, D.; Das, B.; Sarma, D. D.; Rao, C. N. R., *Chemical Physics Letters* 2010, *497,* 66-69.

112. Peng, H.; Mo, Z.; Liao, S.; Liang, H.; Yang, L.; Luo, F.; Song, H.; Zhong, Y.; Zhang, B., *Scientific Reports* 2013, *3,* 1765.

113. Lee, J.; Choi, W., *Journal of The Electrochemical Society* 2015, *162,* A743-A748.

114. Yang, L.; Ravdel, B.; Lucht, B. L., *Electrochemical and Solid-State Letters* 2010, *13,* A95-A97.

115. Park, S. S.; Chu, S.-W.; Xue, C.; Zhao, D.; Ha, C.-S., *Journal of Materials Chemistry* 2011, *21,* 10801-10807.

116. A. Taguet, B. A., Bernard Boutevin, *Advances in polymer science* 2005, *184,* 127-211.

117. Bodenes, L.; Dedryvere, R.; Martinez, H.; Fischer, F.; Tessier, C.; Peres, J. P., *Journal of The Electrochemical Society* 2012, *159,* A1739-A1746.

118. Lin, F.; Nordlund, D.; Markus, I. M.; Weng, T.-C.; Xin, H. L.; Doeff, M. M., *Energy & Environmental Science* 2014, *7,* 3077-3085.

119. Wade, N. S.; Taylor, P. C.; Lang, P. D.; Jones, P. R., *Energy Policy* 2010, *38,* 7180-7188.

120. Le, A. V.; Wang, M.; Shi, Y.; Noelle, D. J.; Qiao, Y., *Journal of Physics D-Applied Physics* 2015, *48*.

121. Wang, M.; Le, A. V.; Shi, Y.; Noelle, D. J.; Yoon, H.; Zhang, M.; Meng, Y. S.; Qiao, Y., *Journal of Materials Science & Technology*.

122. Shi, Y.; Noelle, D. J.; Wang, M.; Le, A. V.; Yoon, H.; Zhang, M.; Meng, Y. S.; Qiao, Y., *ACS Applied Materials & Interfaces* 2016.

123. Kissa, E., *Textile Research Journal* 1996, *66*, 660-668.

124. Washburn, E. W., *Physical Review* 1921, *17*, 273-283.

125. Chibowski, E.; Hołysz, L., *Journal of Adhesion Science and Technology* 1997, *11*, 1289-1301.

126. Xu, B.; Fell, C. R.; Chi, M.; Meng, Y. S., *Energy & Environmental Science* 2011, *4*, 2223-2233.

127. Hy, S.; Liu, H.; Zhang, M.; Qian, D.; Hwang, B.-J.; Meng, Y. S., *Energy & Environmental Science* 2016, *9*, 1931-1954.